THESIS FOR THE DEGREE OF LICENTIATE OF ENGINEERING IN
THERMO AND FLUID DYNAMICS

Advanced Fluid-Structure Interaction Modelling and Simulation for Aerospace Applications

STEFAN NILSSON

Department of Mechanics and Maritime Sciences
Division of Fluid dynamics
CHALMERS UNIVERSITY OF TECHNOLOGY
Gothenburg, Sweden 2022

Advanced Fluid-Structure Interaction Modelling and
Simulation for Aerospace Applications
STEFAN NILSSON

Advanced Fluid-Structure Interaction Modelling and Simulation for Aerospace Applications

STEFAN NILSSON

Department of Mechanics and Maritime Sciences
Division of Fluid dynamics
Chalmers University of Technology

Abstract

Numerical fluid-structure interaction (FSI) methods for the prediction of aeroelastic phenomena are important within aerospace. The continuous development of computer technologies has enabled the use of more advanced FSI methods. The use of advanced methods has the potential to provide more accurate predictions. It also enables simulation of applications for which engineers traditionally have relied upon wind tunnel testing and flight testing, and still do to a large extent. Hence, the use of more advanced FSI methods would limit the need for wind tunnel testing and flight testing, and in extension reduce the lead time and cost of aircraft development.

High Reynolds number flows, involving separated flow, are very challenging to simulate. Hybrid Reynolds-averaged Navier-Stokes (RANS)-large-eddy simulation (LES) techniques provide the possibility to simulate such flows for industrial purposes. Hybrid RANS-LES methods are employed in this thesis for two applications which require turbulence-resolving techniques.

First, the effects of elastic walls on the aeroacoustics in transonic cavity flow are investigated. The prediction of structural vibrations is also important since vibrations may endanger the structural integrity, additionally, vibrations may negatively affect other apparatuses. The features of cavity flow appear in weapon bays and landing gear bays in an aircraft. In a deep cavity, the flow constitutes of broadband and tonal noise, referred to as Rossiter modes. The cavity structure is simulated with a modal-based approach and with a non-modal approach where the equation of motion is solved for all degrees-of-freedom of a reduced order finite element model. The results evince that the aeroacoustic field is altered by the elastic walls. For the investigated case, the energy of the 4th Rossiter mode is depleted and a strong tone is induced at a frequency below the 4th Rossiter mode, which is absent in the rigid cavity; these observations are made with both the structural simulation methods. However, with the non-modal approach, a second strong tone is induced at a frequency above the 4th Rossiter frequency.

The second investigated application is the aeroelastic prediction of a wing at Mach numbers ranging from subsonic to supersonic speeds. The viscous effects become significant at transonic speeds and may provoke shock induced flow separation. It is shown that the viscous effects play an important role under such circumstances and that both static and dynamic structural responses differ significantly depending on whether hybrid RANS-LES or unsteady RANS is employed for the flow simulation.

Keywords: Hybrid RANS-LES, cavity flow, aeroacoustics, aeroelastics, FSI, CFD, CSD

Acknowledgements

I would like to express my sincere gratitude to my supervisors Hua-Dong Yao and Sebastian Arvidson, for their great support and knowledge, which have guided and motivated me throughout this work. I would also like to thank Anders Karlsson for his support and for sharing his expertise. I am also thankful to Peter Eliasson, who always, swiftly and effectively, has helped and supported me.

I am grateful to Sebastian Arvidson, Hans-Peter Magnusson, and Saab Aeronautics, who made my position as an industrial PhD student possible. I would also like to express my thankfulness to all my wonderful colleagues at Saab Aeronautics.

Stefan Nilsson, Linköping, November 2022

Publications

This thesis comprises of two parts. Part I consists of an extended summary and complementary studies. Part II contains the following appended papers:

Paper A Nilsson S., Yao H.-D., Karlsson A., Arvidson S., Effects of Aeroelastic Walls on the Aeroacoustics in Transonic Cavity Flow. *Aerospace,* 9, 716. **2022** *https://doi.org/10.3390/aerospace9110716*

Paper B Nilsson, S., Yao, H.-D., Karlsson, A., Arvidson, S., Effects of Aeroelastic Walls on the Aeroacoustics in Transonic Cavity Flow, Utilising a non-Modal Approach. *Technical report,* **2022**

Paper C Nilsson, S., Yao, H.-D., Karlsson, K., Arvidson, S., Conjunction of Aeroelasticity and Aeroacoustics in Transonic Cavity Flow. *In Proceedings of the International Forum on Aeroelasticity and Structural Dynamics (IFASD), Madrid, Spain, 13–17 June 2022, Paper No. IFASD-2022-020,* **2022**

Paper D Nilsson, S., Yao, H.-D., Karlsson, A., Arvidson, S., Effects of Viscosity and Density on the Aeroelasticity of the ONERA M6 Wing from Subsonic to Supersonic speeds. *In Proceedings of the AIAA Aviation forum, Chicago, IL, USA, 27 June–1 July 2022, Paper No. AIAA 2022-3670,* **2022**

Related puplications:

Arvidson, S., Carlsson, M., Nilsson, S., Effect of LES Length Scale and Numerical Scheme in Hybrid RANS-LES of Free Shear Layer Flows. *In Proceedings of the International Council of Aeronauutical Sciences (ICAS), Stockholm, Sweden, 4–9 September 2022,* **2022**

Contents

Part I

Extended Summary

Chapter 1

Introduction

Fluid-structure interaction (FSI) plays an important role in aerospace applications. Numerical simulations of FSI problems in aerospace are traditionally limited to relatively simple flows, such as attached flows with weak viscous effects. Aeroelastic simulations of flows involving flow separation or strong viscous effects have not been computationally viable. Engineers have, to a large extent relied upon wind tunnel testing and, perhaps foremost, upon flight testing. Wind tunnel testing of aeroelastic models is generally not undertaken without difficulties. Downscaled aeroelastic models must be used, which may also inflict undesirable Reynolds number effects due to the scaling; moreover, measurement obstructions are prevalent. Wind tunnel testing and especially flight testing are expensive and time consuming. Moreover, for flight testing, a prototype must take to the air before the engineers can fully analyse the design. For example, aeroelastic flutter at transonic speeds is difficult to predict with numerical methods and must often be verified by extensive flight testing campaigns, which involve some risks. It is desirable to substitute wind tunnel and flight testing with numerical simulations to be able to assess the design in early stages and to a high level of granularity.

Decades of continuous development of computer technologies has enabled extensive use of numerical simulations. The development of computational fluid dynamics (CFD) and turbulence modelling has followed. Hybrid Reynolds-averaged Navier-Stokes (RANS)-large-eddy simulation (LES) techniques are employed as the main tool for the flow simulations presented in this thesis. Two different cases where sophisticated FSI methods are required are studied. Firstly, the effects of elastic walls on the aeroacoustics in transonic cavity flow. Secondly, the aeroelastics of a wing at transonic speeds. The ensuing sections give a further introduction to these topics.

1.1 Cavity Flow

Internal weapon bays are integral to the stealth operation of combat aircraft. Another example that gives rise to a similar flow field is landing gear bays. The flow in a weapon bay or a landing gear bay is typically what, within the field of fluid dynamics, is referred to as cavity flow. A significant difference between a weapon bay and a landing gear bay is the operational envelope. The landing gears are only intended to be extended at low Mach numbers, whereas the operational envelope for a weapon bay may extend from low subsonic speeds to supersonic speeds.

High Reynolds number cavity flows are inherently unsteady and highly turbulent. Cavity flows are divided into two main categories based on fundamental flow characteristics, namely open and closed cavity flows. The dividing streamline, that is the streamline that separates the re-circulation region from the main flow, in open cavity flow spans the entire cavity length from the leading to the trailing edge, as shown in Figure 1.1 (a).

(a) Open cavity flow.

(b) Closed cavity flow.
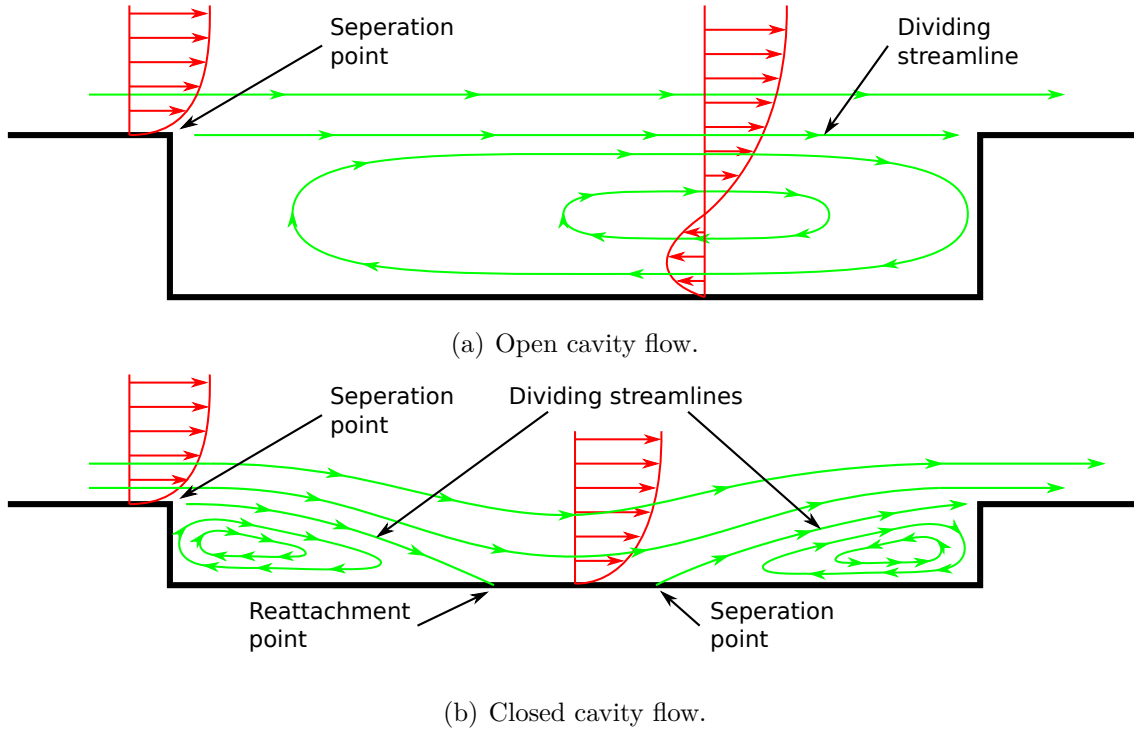
Figure 1.1: Open and closed cavity flow. Green lines depict streamlines and red vectors depict typical streamwise velocity profiles.

A large re-circulation area is formed inside the cavity and a shear layer is present between the re-circulation area and the free-stream flow. In closed cavity flow, Figure 1.1 (b), the flow separates at the leading edge and then reattaches on the cavity floor. The flow then separates once again further downstream and reattaches at the trailing edge. Two re-circulation areas are formed, one in the front and the other in the rear part of the cavity. The distinction between open and closed cavity flow is not necessarily sharp; a third transitional flow state occurs in between. In

transitional cavity flow the dividing streamline bends down into the cavity, but it does not reach the cavity floor; accordingly, the flow does not attach.

As implied in Figure 1.1, closed cavity flow is more likely to occur in a shallow cavity. However, it does not solely depend on the cavity depth. The influence of length-to-depth ratio L/D, width-to-depth ratio W/D, and Mach numbers 0.20–0.95 on the cavity flow characteristics was experimentally investigated by Plentovich et al. [1]. The boundary between open and transitional flow was found at $L/D \approx 6$–8. The boundary between transitional and closed flow was found to be highly dependant on Mach number, L/D, and W/D; the transition boundary was between approximately 9 and 15 in terms of L/D for the investigated cases. It was also found that increasing D or reducing W with constant L/D gives a cavity floor pressure distribution more akin to the distribution in a closed cavity. Furthermore, increasing the Mach number extends the range for L/D for which transitional cavity flow occurs for a given cavity geometry [1].

The length-to-depth ratio for a weapon bay is generally less than 6, and the operational envelope for a weapon bay in a modern combat aircraft, stretches at least up to transonic Mach numbers. Hence, the flow type in a weapon bay is in many cases open cavity flow. The investigated case in this thesis is on open cavity flow.

Cavity flows have been extensively investigated since the 1950s, some early studies were by Roshko (1955) [2], Krishnamurty (1955) [3], Dunham (1962) [4], Plumblee et al. (1962) [5], Rossiter (1964) [6], and East (1966) [7]. It was observed that the flow in an open cavity generates broadband and tonal noise. The tonal noise is also known as Rossiter modes, named after the work by Rossiter [6]. In 1962, Plumblee et al. [5] suggested that the observed tones were due to cavity resonance. They computed the acoustic resonance and compared with experiments. They also suggested that the spectrum of boundary layer fluctuations upstream of the cavity is driving the acoustic resonance. Come 1964, Rossiter [6] deemed this hypothesis untenable, partly because of the findings by Krishnamurty [3] who showed that the tonal noise was present even though the approaching boundary layer is laminar. Rossiter concluded that acoustic resonance appears to be integral to the explanation of the tonal noise, but the driving force is the shear layer spanning the cavity, rather than the boundary layer upstream of the cavity. Rossiter investigated a whole host of cavities with varying geometrical parameters and Mach numbers. Based on the data, he could formulate an semi-empirical formula to determine the frequency f of the n-th mode:

$$f_n = \frac{U_\infty(n-\gamma)}{L(\frac{1}{\kappa} + M_\infty)}, \quad 0 \le \gamma < 1, \quad 0 < \kappa \le 1 \tag{1.1}$$

According to Rossiter's formula, the n-th mode frequency depends on both the free-stream velocity magnitude U_∞ and the free-stream Mach number M_∞, thus, the free-stream sound speed. The constant γ is the phase shift between the vortex shedding and the acoustic wave. The other constant, κ, is the travel speed of the vortices, in terms of the proportion of the free-stream speed. Rossiter's formula can be used as a rough estimate of the Rossiter frequencies, the accuracy can vary

between the modes for a given cavity and flow conditions. The formula merely include the most important parameters; the cavity depth is for example ignored, which is more important for some cavity flows than others. Moreover, the formula does not tell anything about the magnitude of the tones, or if a tone is active or not.

The acoustic feedback loop in a cavity is complex, and a unified analytical theory has not yet been presented. Several attempts have been made after Rossiter to improve the prediction of Rossiter modes, often by including more variables, for instance by Tam and Block [8]. The Rossiter mode frequencies and strength are generally not constant over time. The time variance of the modes can be large enough to change which mode is the dominant. This phenomenon is referred to as mode switching, which means that the energy of a mode decreases whilst the energy of another mode increases [9, 10]. Mode switching is related to the shape of the shear layer.

Many of the fundamental studies are focusing on ideal cavities (perfectly rectangular cavities), which is important for the understanding of cavity flows. Nonetheless, a cavity in a real-world application is seldom ideal. A weapon bay is generally geometrically complex. The geometry does not have to be rectangular and it may contain various apparatuses, such as electrical wiring, hydraulic lines, store ejectors, and a weapon before its deployment. The complex shape requires experimental and/or numerical investigations of the flow.

The energetic pressure fluctuations in a cavity interact with the structure. This has several potential implications. Static and dynamic deformations may be detrimental to the structural integrity. The structure must withstand the static loads and protracted vibrations may lead to acoustic fatigue. Furthermore, high vibration levels may be detrimental to other apparatuses as the vibrations propagate in the structure. The strong acoustic field generated by a cavity may also lead to unacceptable noise levels, particularly for manned aircraft. The interaction may change the acoustic field, moreover, the interaction between the structure and fluid is bidirectional. This means that coupled CFD and computational structural dynamics (CSD) simulations must be undertaken to investigate the potential implications. This topic is not well-explored, at least not in the open literature. The appended papers are novel investigations of transonic cavity flow with an elastic cavity. In Paper A [11], B [12], and C [13] a cavity is studied at the same flow conditions using hybrid RANS-LES, but different numerical methods are used for the structural simulation. Paper A is an extended version of Paper C. The methods for flow simulation and structural simulation is presented in Chapter 2.

1.2 Classical Aeroelasticity

The aeroelasticity of a wing is a quintessential FSI problem within aerospace. Classical aeroelasticity has been studied since the dawn of aviation. Both static and dynamic aeroelastic phenomena with ominous characteristics or with a catastrophic failure as a result were observed early on, and engineers have been grappling with these issues since. Nonetheless, even if the fundamental phenomena relating to classical aeroelasticity are well understood, it is challenging to predict aeroelastic

behaviour under certain conditions. The presence of shock-waves on a wing surface in a transonic flow makes viscous effects important. The shock wave/boundary-layer interaction (SWBLI) [14] may affect the shock wave position and the shock may provoke a shock induced flow separation. In the case of a flow separation, turbulence-resolving techniques become essential for the prediction of aeroelastic behaviour [15].

An aircraft is subjected to aerodynamic forces that deform the lifting surfaces. Since the aircraft's geometrical shape is changing, the flow over the lifting surfaces will change and hence the aerodynamic forces are altered; the interaction is bidirectional. To accurately predict the lift and drag of an elastic wing, the wing's elasticity must be considered. This is a classical static aeroelastic problem of aeroplanes.

Aerodynamic flutter is a self-excited dynamic instability, for which the aerodynamic forces couple with the inertial and elastic forces of the wing [16]. The onset of flutter is governed by the dynamic pressure. Flutter is detrimental to an airframe, the amplitude of the oscillations increases for each cycle until the structure's failure point is reached. Hence, it is easy to understand that flutter is highly undesirable. It must be ascertained that an aircraft does not encounter flutter conditions within the operational envelope.

Viscous effects are often negligible for classical wing aeroelasticity at subsonic and supersonic speeds with attached flow. For such flows it is commonplace to employ inviscid flow theory, for example, the inviscid Euler equations (IEE). In Paper D [17] the viscous effects are investigated. An aeroelastic wing is simulated with hybrid RANS-LES and with the IEE at Mach numbers of 0.6-1.1. A few of the cases were also simulated with unsteady RANS (URANS). The difference regarding aeroelastic responses between hybrid RANS-LES and URANS is anticipated to be small for attached flow, whereas a significant difference is expected for the IEE simulations. Separated flow was obtained in a few of the investigated cases; here, a difference between hybrid RANS-LES and URANS is likely [15]. However, some inadequacies regarding the methodology resulted in a lack of resolved turbulence, which further is likely to give inadequate results. A complementary study of a single transonic case was therefore undertaken, which is presented in Chapter 4. Simulations with URANS and hybrid RANS-LES on a rigid and elastic wing are compared. The simulations are performed on a finer CFD grid and a different turbulence model and numerical scheme are employed for the hybrid RANS-LES simulations.

1.3 Objectives and Motivation

The overall objective is to develop an understanding and gain experience of advanced fluid-structure interaction methods and aeroacoustics. In particular, aerospace applications that require fluid-structure interaction simulation in combination with turbulence-resolving techniques.

The main objective is to investigate potential effects of elastic walls on the aeroacoustics in transonic cavity flow. This topic is not well-covered in the scientific literature. The industrial need of insights into cavity flows and how they affect the structure and, in turn, how the elastic structure affects the aeroacoustic near- and far-field is also part of the motivation behind this work. A sub-objective is to

investigate methodologies for structural simulation of the cavity, including a modal-based approach, a non-modal approach, and investigation of finite element model reduction methods.

A second objective is to investigate and gain insights to viscous effects, and the effects of shock induced flow separation, on aeroelastic behaviour of an aeroelastic wing.

1.4 Thesis Outline

The thesis is organised as follows:

Chapter 1 presents the motivation behind the project and the reader is introduced to cavity flows and classical aeroelasticity.

Chapter 2 presents the numerical methods for flow simulation and for structural simulation.

Chapter 3 presents complementary studies which relate to Paper A, B, and C. Some important aspects of the finite element model are discussed. An investigation of far-field noise of a rigid and an elastic cavity is also presented. The source terms for the Ffowcs Williams and Hawkings acoustic analogy are extracted from the results presented in Paper A.

Chapter 4 presents a complementary investigation of the aeroelastic wing, the investigation relates to Paper D. An improved methodology is used for the hybrid RANS-LES simulation. The results of the rigid and the aeroelastic wing are compared with corresponding URANS simulations.

Chapter 5 presents a summary of the thesis, including the appended Papers A–D.

Chapter 2

Numerical Methods

2.1 Numerical Methods for Flow Simulation

This section presents the governing equations and a brief introduction to turbulence modelling.

2.1.1 Governing Equations

The Navier-Stokes equations for unsteady compressible flow are:

$$\frac{\partial \rho}{\partial t} + \frac{\partial (\rho u_i)}{\partial x_i} = 0, \tag{2.1}$$

$$\frac{\partial (\rho u_i)}{\partial t} + \frac{\partial (\rho u_i u_j)}{\partial x_j} = -\frac{\partial p}{\partial x_i} + \frac{\partial \sigma_{ij}}{\partial x_j}, \tag{2.2}$$

$$\frac{\partial (\rho e_0)}{\partial t} + \frac{\partial (\rho e_0 u_j)}{\partial x_j} = -\frac{\partial p u_j}{\partial x_j} + \frac{\partial}{\partial x_j}\left[\kappa \frac{\partial T}{\partial x_j} + u_i \sigma_{ij}\right]. \tag{2.3}$$

Here, ρ is density, u is the velocity components, x is the coordinates, p is pressure, T is temperature, and t is time. The thermal conductivity $\kappa = (C_p \mu)/P_r$, where C_p is the specific heat capacity, μ is the molecular viscosity, and P_r is the Prandtl number. The total energy $e_0 = e + (u_i u_i)/2$, where the internal energy for a perfect gas $e = C_V T$. The specific heat capacity for constant volume $C_V = R/(\gamma - 1)$. For all flows in this thesis, the specific gas constant $R = 287$ J $\cdot$ kg^{-1}K^{-1}, and the heat capacity ratio $\gamma = 1.4$. For a Newtonian fluid the viscous stress tensor is:

$$\sigma_{ij} = \mu\left(\frac{\partial u_i}{\partial x_j} + \frac{\partial u_j}{\partial x_i} - \frac{2}{3}\frac{\partial u_k}{\partial x_k}\delta_{ij}\right). \tag{2.4}$$

Here, $\delta_{i,j}$ is the Kronecker delta function. The equation of state is:

$$p = (\gamma - 1)\left[\rho e_o - \frac{1}{2}\rho u_i u_i\right]. \tag{2.5}$$

2.1.2   Turbulence Modelling

Direct numerical simulation (DNS) of the Navier-Stokes equations is generally not computationally viable, especially not for industrial applications. No turbulence model is used in DNS, instead, all relevant temporal and spatial length scales must be resolved. The temporal and spatial requirements are determined by the Kolmogorov time and length scales [18]. The temporal and spatial scale requirements can be alleviated by spatial filtering of the Navier-Stokes equations.

The Reynolds-averaged Navier-Stokes (RANS) equations are formed, as the name implies, by an averaging operation. The RANS equations contain additional terms in the momentum equation, known as Reynolds stresses. The Reynolds stresses are unknown and need to be modelled by a turbulence model to close the set of equations. By retaining the transient terms in the RANS equations, the mean flow transients can be captured in time, that is, unsteady RANS (URANS) [19]. For example, the periodic vortex shedding downstream of a cylinder can be simulated with URANS.

In large-eddy simulation (LES), the largest scales of the turbulent spectrum are resolved, whereas the small scales are filtered out. Similar to RANS, the filtering leads to additional terms, which for LES are known as sub-grid scale stresses. The sub-grid scale stresses are unknown and must be modelled to close the set of equations. The term "sub-grid scale" stems from the fact that filtering of the equations is related to the local grid resolution; scales smaller than the local grid resolution are modelled. The grid resolution also sets a requirement on the time step. Moreover, the time step must be sufficiently small to capture the resolved scales in the turbulent spectrum. Compared with RANS modelling, LES requires a much smaller time step and a much finer grid resolution [20].

The idea of hybrid RANS-LES is to exploit the virtues of RANS in near-wall regions, whereas LES is used in off-wall regions. By doing so, the requirement of an extremely fine grid resolution in the near-wall regions is alleviated. However, it also means that there must be an interface between the RANS mode and the LES mode. Hybrid RANS-LES turbulence models suffer from several issues relating to the interface. Various formulations of the interface have been proposed in an effort to mitigate the effects of the interface [19, 20].

The delayed detached-eddy simulation (DDES) [21] based on Spalart-Allmaras (SA) one-equation turbulence model [22], and SA-based improved DDES (IDDES) [23] are employed in this thesis.

2.2   Numerical Methods for Structural Simulation

Finite element (FE) models are generally too large for direct computation of the governing equation. Therefore, it is customary to employ a reduction technique to decrease the order of the structural model. For classical wing aeroelasticity the most prevalent reduction technique is a modal decomposition method. Modal decomposition is especially suitable for this type of problems. The first bending and torsional modes of a lifting surface—such as a wing or a fin—have a predominant role to the aeroelastic behaviour. Thus, it is often sufficient to represent the structure with

a few eigenmodes. For other structures, such as a cavity where a wide range of eigenmodes are significant, other reduction techniques may be preferable.

Modal decomposition is employed for the cavity in Paper A and C, and also for the wing in Paper D. In Paper B a reduced order FE model is used, for which the equation of motion is directly solved. The ensuing sections introduce the employed methods.

2.2.1 Governing Equations

The governing equation for the time dependant structural coordinates $\boldsymbol{x}(t)$ for the full order system is given by the equation of motion:

$$\boldsymbol{M}\ddot{\boldsymbol{x}}(t) + \boldsymbol{C}\dot{\boldsymbol{x}}(t) + \boldsymbol{K}\boldsymbol{x}(t) = \boldsymbol{f}(t). \tag{2.6}$$

Here, $\boldsymbol{M}$ is the mass matrix, $\boldsymbol{C}$ is the damping matrix, $\boldsymbol{K}$ is the stiffness matrix, and $\boldsymbol{f}(t)$ is the external force acting on the system. It is assumed that the systems energy dissipation can be described by the viscous damping which is proportional to a linear combination of the mass and stiffness matrices. That is the so-called Rayleigh damping:

$$\boldsymbol{C} = \alpha\boldsymbol{M} + \beta\boldsymbol{K}, \quad \alpha, \beta \geq 0. \tag{2.7}$$

The damping is thus determined by the Rayleigh damping coefficients α and β. The equation of motion—Equation (2.6)—has the same form if a reduced order FE model is used, it is only the order of the matrices that is reduced. The component mode synthesis by Craig and Bampton [24] is employed for the reduction of the matrices in this thesis. Craig and Bampton's method is underpinned by the exact static condensation by Guyan [25]. The forthcoming section explains the exact static condensation, followed by Craig and Bampton's method.

2.2.2 Exact Static Condensation

Exact static condensation [25]—also called Guyan condensation—is based on the static equation of equilibrium for the full order system:

$$\boldsymbol{K}\boldsymbol{x} = \boldsymbol{f}. \tag{2.8}$$

The stiffness matrix is partitioned into sub-matrices. Each degree-of-freedom that is condensed are referred to as a slave and the retained degrees-of-freedom are referred to as masters, indicated by subscripts s and m, respectively. After separating the slaves and the masters, Equation (2.8) can then be written as:

$$\begin{bmatrix} \boldsymbol{K}_{mm} & \boldsymbol{K}_{ms} \\ \boldsymbol{K}_{sm} & \boldsymbol{K}_{ss} \end{bmatrix} \begin{Bmatrix} \boldsymbol{x}_m \\ \boldsymbol{x}_s \end{Bmatrix} = \begin{Bmatrix} \boldsymbol{f}_m \\ \boldsymbol{f}_s \end{Bmatrix}. \tag{2.9}$$

Multiplication of the left-hand side expands Equation (2.9):

$$\boldsymbol{K}_{mm}\boldsymbol{x}_m + \boldsymbol{K}_{ms}\boldsymbol{x}_s = \boldsymbol{f}_m, \tag{2.10}$$

$$\boldsymbol{K}_{sm}\boldsymbol{x}_m + \boldsymbol{K}_{ss}\boldsymbol{x}_s = \boldsymbol{f}_s. \tag{2.11}$$

By rearranging Equation (2.11), the slave displacement vector $\boldsymbol{x}_s$ can be expressed in terms of the master displacement vector $\boldsymbol{x}_m$:

$$\boldsymbol{x}_s = -\boldsymbol{K}_{ss}^{-1}\boldsymbol{K}_{sm}\boldsymbol{x}_m + \boldsymbol{K}_{ss}^{-1}\boldsymbol{f}_s. \tag{2.12}$$

The displacements of the slaves are described by two terms. The first term emerges from the displacement of the masters, that is the so-called attached displacements. The second term results from the external forces acting on the slaves and is referred to as relative displacements [26]. Combining Equations (2.12) and (2.10) gives:

$$\boldsymbol{K}_R\boldsymbol{x}_m = \boldsymbol{f}_R, \tag{2.13}$$

where,

$$\boldsymbol{K}_R = \boldsymbol{K}_{mm} - \boldsymbol{K}_{ms}\boldsymbol{K}_{ss}^{-1}\boldsymbol{K}_{sm}, \tag{2.14}$$

$$\boldsymbol{f}_R = \boldsymbol{f}_m - \boldsymbol{K}_{ms}\boldsymbol{K}_{ss}^{-1}\boldsymbol{f}_s. \tag{2.15}$$

In order to derive the relation for the displacement between masters and slaves, it is necessary to assume a zero external force applied to the slave nodes. Letting $\boldsymbol{f}_s = \boldsymbol{0}$, Equation (2.12) becomes:

$$\boldsymbol{x}_s = \boldsymbol{R}_G\boldsymbol{x}_m, \tag{2.16}$$

where $\boldsymbol{R}_G$ is the Guyan condensation matrix, which is defined as:

$$\boldsymbol{R}_G = -\boldsymbol{K}_{ss}^{-1}\boldsymbol{K}_{sm}. \tag{2.17}$$

The displacement vector can be expressed as:

$$\boldsymbol{x} = \begin{Bmatrix} \boldsymbol{x}_m \\ \boldsymbol{x}_s \end{Bmatrix} = \boldsymbol{T}_G\boldsymbol{x}_m. \tag{2.18}$$

Here, $\boldsymbol{T}_G$ is the coordinate transformation matrix, also called the global mapping matrix:

$$\boldsymbol{T}_G = \begin{Bmatrix} \boldsymbol{I} \\ \boldsymbol{R}_G \end{Bmatrix}. \tag{2.19}$$

Here, $\boldsymbol{I}$ is the identity matrix. The coordinate transformation matrix relates the responses of all degrees-of-freedom to the responses at the masters. Substituting Equation 2.18 into Equation 2.8 and premultiplying with the transpose of $\boldsymbol{T}_G$ gives:

$$\boldsymbol{K}_G\boldsymbol{x}_m = \boldsymbol{f}_G. \tag{2.20}$$

Here, $\boldsymbol{K}_G$ is the reduced stiffness matrix and $\boldsymbol{f}_G$ is the equivalent force vector acting at the masters, defined as:

$$\boldsymbol{K}_G = \boldsymbol{T}_G^T \boldsymbol{K} \boldsymbol{T}_G, \tag{2.21}$$

$$\boldsymbol{f}_G = \boldsymbol{T}_G^T \boldsymbol{f}. \tag{2.22}$$

The reduced stiffness matrix and the force vector may also be written in terms of the sub-matrices and vectors:

$$\boldsymbol{K}_G = \boldsymbol{K}_{mm} - \boldsymbol{K}_{ms} \boldsymbol{K}_{ss}^{-1} \boldsymbol{K}_{sm}, \tag{2.23}$$

$$\boldsymbol{f}_G = \boldsymbol{f}_m - \boldsymbol{K}_{ms} \boldsymbol{K}_{ss}^{-1} \boldsymbol{f}_s. \tag{2.24}$$

The term "exact static condensation" stems from the fact that dynamic effects are ignored in the condensation, and the condensation is mathematically exact for a static system. The Guyan condensation may be used for a dynamic system, but is then no longer exact. The stiffness matrix $\boldsymbol{K}$ in Equation (2.21) can be replaced by the mass matrix $\boldsymbol{M}$ to compute the reduced mass matrix $\boldsymbol{M}_G$.

2.2.3 Component Mode Synthesis by Craig and Bampton

The component mode synthesis (CMS) by Craig and Bampton [24] is based on the exact static condensation by Guyan. The CMS provides a coupling between the internal variables and the interface degrees-of-freedom and compensates for the neglected inertia terms in the Guyan condensation. The reduction is augmented with a set of generalised coordinates ξ, which represent the amplitude of a set of eigenmodes of the slave model, which are derived with the masters fixed. Equation (2.6) is partitioned, similar to Equation (2.9), but including the mass matrix. Setting $\boldsymbol{x}_m = \boldsymbol{0}$ and $\boldsymbol{f}_s = \boldsymbol{0}$ in the partitioned equation of equilibrium result in the eigenvalue problem:

$$\boldsymbol{K}_{ss} \boldsymbol{\Phi} = \lambda \boldsymbol{M}_{ss} \boldsymbol{\Phi}. \tag{2.25}$$

The eigenvalue problem is solved for eigenvalues λ and eigenvectors $\boldsymbol{\Phi}$. A set of eigenmodes is retained as an additional basis to the approximation of the slave model. For CMS, Equation (2.12) becomes:

$$\boldsymbol{x}_s = -\boldsymbol{K}_{ss}^{-1} \boldsymbol{K}_{sm} \boldsymbol{x}_m + \sum \Phi_i \xi_i = \boldsymbol{R}_G \boldsymbol{x}_m + \boldsymbol{\Phi} \boldsymbol{\xi}. \tag{2.26}$$

The CMS coordinate transformation matrix is:

$$\boldsymbol{T}_{CMS} = \begin{bmatrix} \boldsymbol{I} & \boldsymbol{0} \\ \boldsymbol{R}_G & \boldsymbol{\Phi} \end{bmatrix} \tag{2.27}$$

The structural coordinates are given by:

$$\begin{Bmatrix} \boldsymbol{x}_m \\ \boldsymbol{x}_s \end{Bmatrix} = \boldsymbol{T}_{CMS} \begin{Bmatrix} \boldsymbol{x}_m \\ \boldsymbol{\xi} \end{Bmatrix}. \tag{2.28}$$

The selection of masters plays an important role to the accuracy of the CMS (and Guyan condensation). Furthermore, the accuracy depends upon the selection of retained eigenmodes. All eigenmodes with frequencies of interest should be retained to assure a sufficient accuracy [27]. The reduction of the matrices is straightforward, however, the selection of masters is not obvious. The ensuing section discusses the selection of masters.

2.2.4 Selections of Masters

The valid eigenvalue range of the Guyan condensation is $(0, \lambda_c)$ [26]. The cut-off eigenvalue λ_c is equal to the lowest eigenvalue of the slave model, that is, the full order model with all the masters constrained. The approximate eigenvalue errors due to Guyan condensation are inversely proportional to the cut-off eigenvalue. Hence, the accuracy of Guyan condensation increases as λ_c increases. The fundamental requirement to the selection of masters is therefore to maximise the lowest eigenvalue of the slave model. Notwithstanding that this fundamental requirement is dedicated to Guyan condensation, it is still valid for its variants and all physical-type dynamic condensation methods.

Various qualitative guidelines have been proposed. Levy [28] proposed that the masters should be selected based on the largest entries of the mass matrix, and degrees-of-freedom that have the largest displacements. Rather than focusing on all individual degrees-of-freedom, Ramsden and Stoker [29] selected the masters in areas of the structure that are associated with large concentrations of mass. Areas that are more flexible relative to other mass concentrations should be selected first. Popplewell et al. [30] proposed a guideline in terms of strain energy conservation. The disadvantage of many proposed qualitative guidelines is that they require prior knowledge of the system response. For simple structures the required information might be known, but for complex structures, that is generally not the case [26].

Contrary to the qualitative guidelines, quantitative guidelines can generally be implemented in a programme code for an automatic selection of masters. Several proposed algorithms are based on the ratio of the diagonal elements of the stiffness and mass matrices. Shah and Raymond [31] proposed an algorithm that condenses the slaves one by one directly from the full stiffness and mass matrices. Matta [32] proposed a scheme where a certain number of degrees-of-freedom with the smallest ratio are selected as masters. A comprehensive study of Shah's and Matta's algorithms was undertaken by Suarez and Singh [33]. They concluded that Shah and Raymond's algorithm is better than Matta's algorithm, though the former is more computationally expensive than the latter. Algorithms based on the ratio of the diagonal elements are applicable to all structures, but might not be suitable for structures with irregular mass distribution. In such cases there is a risk of concentrating the bulk of masters in regions with significant masses [34, 35]. However, if the structure has relatively uniform mechanical and geometrical proprieties this type

of scheme provides excellent results. Shah and Raymond's algorithm is described in detail and employed in Paper B.

Structural models which are symmetric regarding geometrical and material properties in two or three directions often have repeated eigenfrequencies, for instance a square plate. For such structures, the symmetry should be considered in the selection of masters to preserve the symmetry features in the reduced model [26].

It is not always possible to follow all guidelines regarding selection of masters. In some cases, certain degrees-of-freedom must be kept in the master set for practicality purposes, regardless whether or not they satisfy the guidelines. It could for example be degrees-of-freedom at which external forces act, prescribed displacements, or at which responses are of interest.

The selection of masters has a significant influence on the accuracy. The selection should result in a reduced model as accurate as possible. As the number of masters increases, the dynamic characteristics of the reduced model will steadily approach those of the full model; however, it increases the computational effort. It may not always be computationally viable if all guidelines considering accuracy are followed. In such cases, there must be a trade-off between accuracy and computational effort.

2.2.5 Modal Decomposition

The modal decomposition is based on the eigenvalue problem of the equation of motion, Equation (2.6), of the full order model. The decomposition results in a set of linear equations that describes the structural coordinates $\boldsymbol{x}(t)$. The coordinates are represented by normal mode shapes (eigenvectors) $\boldsymbol{\phi}_k$ and modal coordinates $q_k(t)$:

$$\boldsymbol{x}(t) = \boldsymbol{x}_0 + \sum_{k=1}^{N_m} q_k(t)\boldsymbol{\phi}_k. \tag{2.29}$$

The subscript k indicates the k-th mode, and $\boldsymbol{x}_0 = \boldsymbol{x}(t=0)$ is the initial condition. The external forces and the damping are both zero for the special case of free vibration, then the equation of motion reduces to a generalised eigenvalue problem:

$$\boldsymbol{K}\boldsymbol{\phi}_k = \omega_k^2 \boldsymbol{M}\boldsymbol{\phi}_k, \quad k \in [1, N]. \tag{2.30}$$

The solution to the eigenvalue problem gives N eigenvectors and the associated angular eigenfrequencies ω_k. The value of N is equal to the dimension of $\boldsymbol{x}$, which is the total number of structural degrees-of-freedom. It is here assumed that the normal mode shapes and corresponding frequencies are ordered as $\omega_1 < \omega_k < \omega_{k+1} < , \cdots, < \omega_{N-1} < \omega_N$. The normal mode shapes satisfy the orthogonality conditions:

$$\boldsymbol{\phi}_j^T \boldsymbol{M}\boldsymbol{\phi}_k = a_k \delta_{jk}, \tag{2.31}$$

$$\boldsymbol{\phi}_j^T \boldsymbol{K}\boldsymbol{\phi}_k = a_k \omega_k^2 \delta_{jk}. \tag{2.32}$$

The normalisation constant a_k is known as the generalised mass for the k-th mode, and δ is the Kronecker delta function. The full system with N degrees-of-freedom can be truncated at order $N_m \ll N$. The equation of motion is thus with the truncated modal basis reduced to a set of N_m scalar equations, which are coupled only through the external force term. The equation of motion can be rewritten by combining Equation (2.29) and the orthogonality conditions, Equations (2.31) and (2.32), and pre-multiplying Equation (2.6) with the transpose of $\boldsymbol{\phi}_k$:

$$a_k \ddot{q}_k + 2\zeta_k a_k \omega_k \dot{q}_k + a_k \omega_k^2 q_k = Q_k, \quad k \in [1, N_m], \tag{2.33}$$

$$Q_k = \boldsymbol{\phi}_k^T \boldsymbol{f}. \tag{2.34}$$

Here ζ_k is the damping ratio for mode k, and Q_k is known as the generalised force. A Newmark's time-integration scheme is applied to Equation (2.33):

$$\dot{q}_k^{n+1} = \dot{q}_k^n + \Delta t(1 - \gamma)\ddot{q}_k^n + \Delta t \gamma \ddot{q}_k^{n+1}, \tag{2.35}$$

$$q_k^{n+1} = q_k^n + \Delta t \dot{q}_k^n + \Delta t^2 \left(\frac{1}{2} - \sigma\right)\ddot{q}_k^n + \Delta t^2 \sigma \ddot{q}_k^{n+1}. \tag{2.36}$$

Here Δt is the time step and n is the time step number. Setting the parameters $\gamma = \frac{1}{2}$ and $\sigma = \frac{1}{6}$ corresponds to a linear interpolation of the modal acceleration $\ddot{q}(t), t \in [t^n, t^{n+1}]$. Combining Equations (2.33), (2.35), and (2.36) the modal acceleration $\ddot{q}_k^{n+1}$ can be computed. Subsequently, the acceleration can be substituted back into Equations (2.35) and (2.36) which gives the modal velocity and the modal coordinate.

Chapter 3

Aeroelasticity of the M219 Cavity

T his chapter presents complementary studies on the M219 cavity [36], which relate to Paper A, B, and C. First, grid resolution aspects of the finite element model of the cavity are discussed. Secondly, the far-field noise stemming from the elastic and rigid cavity is predicted using an acoustic analogy. A brief introduction is also given to acoustic analogies.

3.1 Finite Element Models

3.1.1 Dynamic Considerations

The presence of high frequency aeroacoustic waves that stimulate the structure entails a requirement on the spatial resolution of a structural model. The grid must be fine enough to capture the pressure fluctuations acting on the structure. The maximum resolved frequency f_{max} can be computed from:

$$\lambda = \frac{c_0}{f_{max}}, \tag{3.1}$$

$$\Delta s = \frac{\lambda}{n}. \tag{3.2}$$

Here, λ is the wavelength, c_0 is the speed of sound (phase velocity), f_{max} is the cut-off frequency, n is the number of elements per wavelength, and Δs is the element edge length. The number of elements per wave length must be at least four to capture a wave, this is illustrated in Figure 3.1. If only two or fewer elements span a wave as in Figure 3.1 (a), merely the static pressure is captured (also depending on the phase). In Figure 3.1 (b) there is four elements per wave length and the characteristics of the wave is captured. Increasing the number of elements per wave length significantly increases the resolution of the wave, as seen in Figure 3.1 (c)–(d). The cut-off frequency should be at least equal to the highest significant frequency of the acoustic field.
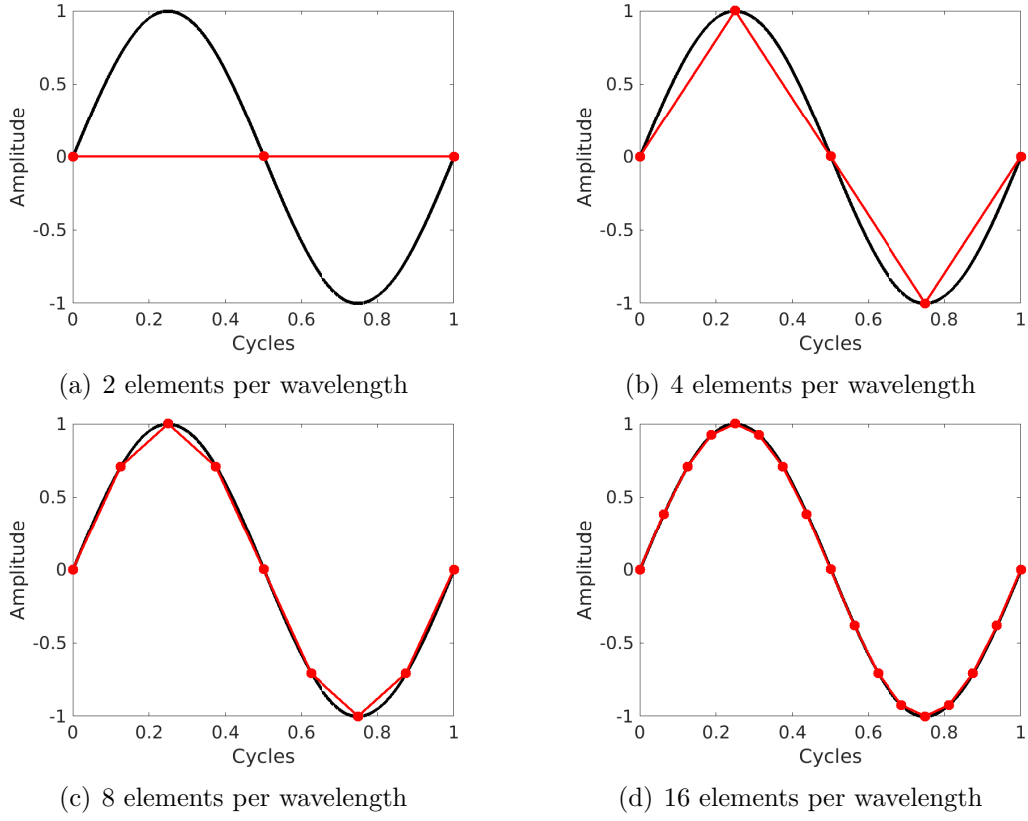
(a) 2 elements per wavelength

(b) 4 elements per wavelength

(c) 8 elements per wavelength

(d) 16 elements per wavelength

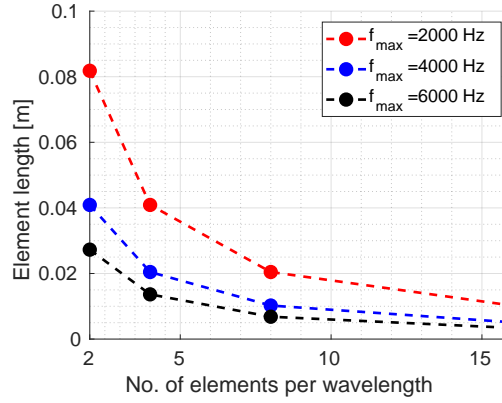**Figure 3.1:** Illustration of wave resolution depending on the number of elements per wavelength.

Figure 3.2: Element length as function of number of elements per wavelength, for three different cut-off frequencies.

Figure 3.2 shows the element edge length as a function of n, for three different cut-off frequencies. A sound speed of $c_0 = 327$ ms^{-1} is used, which is the same as for the cavity flow in Paper A, B, and C. The higher values for f_{max} and n, the smaller elements. The accuracy generally increases as the element size decreases, however, the size of the FE model swiftly grows. The total number of entries in the system matrices grows with the square of the number of grid points in the FE model.

18

3.1.2 Finite Element model of the Cavity

A static grid convergence study for the FE model of the cavity has been undertaken. Two different pressure distributions were applied to the cavity walls. First, a spatially uniform pressure distribution and secondly an instantaneous pressure distribution from a time dependant CFD simulation. The latter was partly performed to visually get a perception of the pressure distribution after it was mapped onto the FE grid.

A first-order element only has corner nodes, whereas a second-order element has corner and mid-edge nodes. Hence, the edges of a first-order element is always straight, whereas the edges of a second-order element can curve. The accuracy of a second-order element is generally higher, although the accuracy of the FE model highly depends on the element size as well.

The FE model consists of first-order quadrilateral shell elements (called CQUAD4 in MSC Nastran [37]). Young's modulus is $70 \cdot 10^9$ kg·m^{-1}s^{-2}, Poisson's ratio is 0.33, the material density is 2700kg·m^{-3}, and the shell thickness is 1.5 mm. The length of the M219 cavity is 0.5080 m, the depth and the width are 0.1016 m. Each node comprises six degrees-of-freedom—three translational and three rotational. The material and geometrical properties are the same as those used in Paper A, B and C. In Paper A, the rationale for choosing the material and geometrical properties of the cavity is further elaborated upon.

Table 3.1: The number of elements across the cavity width and the total number of elements in the FE models.

FE Model	No. of elements across cavity	Total No. of elements	FE Grid	No. of elements across cavity	Total No. of elements
1	4	272	12	15	3825
2	5	425	13	16	4352
3	6	612	14	17	4913
4	7	833	15	18	5508
5	8	1088	16	19	6137
6	9	1377	17	20	6800
7	10	1700	18	30	15300
8	11	2057	19	40	27200
9	12	2448	20	79	106097
10	13	2873	21	80	108800
11	14	3332			

The spatially uniform pressure applied to the cavity walls is 2.3 MPa, which is much higher than the actual peak pressures for the cavity in the transonic flow in Paper A–C; the pressure is set high to obtain larger displacements for the static solution. The maximum displacements for 21 different element sizes were examined for the spatially uniform distribution. The coarsest grid consists of elements with an edge length of 25.40 mm and the finest has an edge length of 1.27 mm. The two finest grids have smaller elements than the CFD surface grid. To that end, only the 19 FE models with edge lengths greater than the CFD surface grid were employed for the CFD pressure distribution. The number of elements in the 21 FE models are

given in Table 3.1. The number of elements across the cavity width are also given in the Table 3.1, rather than the element edge lengths.

Figure 3.3 shows the CFD pressure distribution mapped onto grids 3, 7, 17, and 19. In this, and ensuing figures, of the cavity the cavity side walls are folded outwards to enable a two-dimensional view of the cavity. Small features of the pressure distribution are highly detailed for grid 19 (Figure 3.3 (d)), whereas the features are very poorly detailed for grid 3, as seen i Figure 3.3 (a).

(a) FE model 3.

(b) FE model 7.

(c) FE model 17.
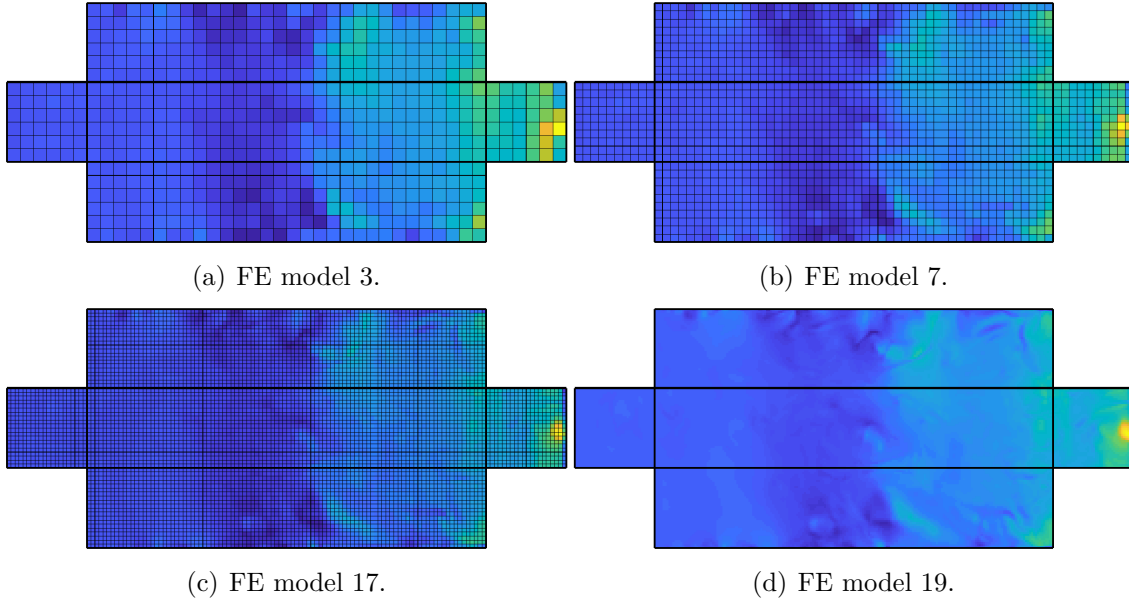
(d) FE model 19.

Figure 3.3: The CFD pressure distribution mapped onto the FE grids. The grid is not shown for FE model 19.
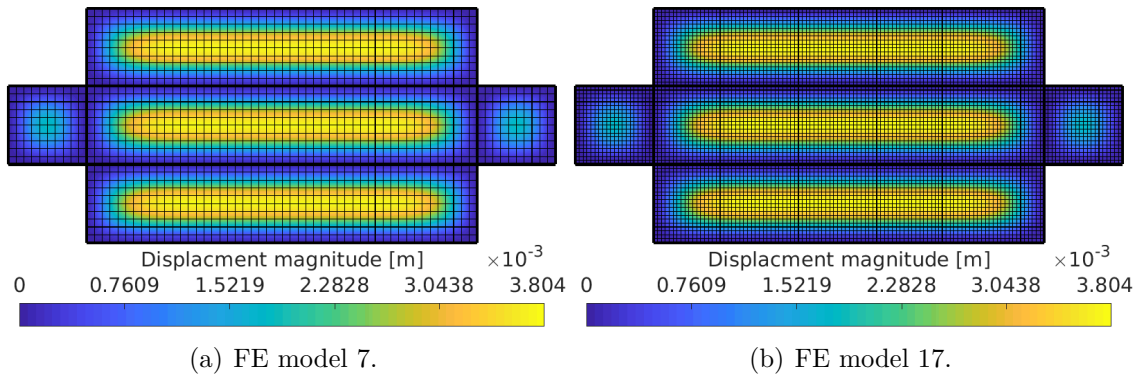

(a) FE model 7.

(b) FE model 17.

Figure 3.4: Static displacement magnitudes of the cavity with the spatially uniform pressure distribution.

The static deformation problem was solved using MSC Nastran [37]. Figure 3.4 shows the static deformations for grids 7 and grid 17, using the spatially uniform pressure distribution. Corresponding deformations for the CFD distribution are shown in Figure 3.5. For the examples shown in the figures, deformations are similar.

The reason for showing grids 7 and 17 in particular, is because these grids are used in Paper A, B and C.
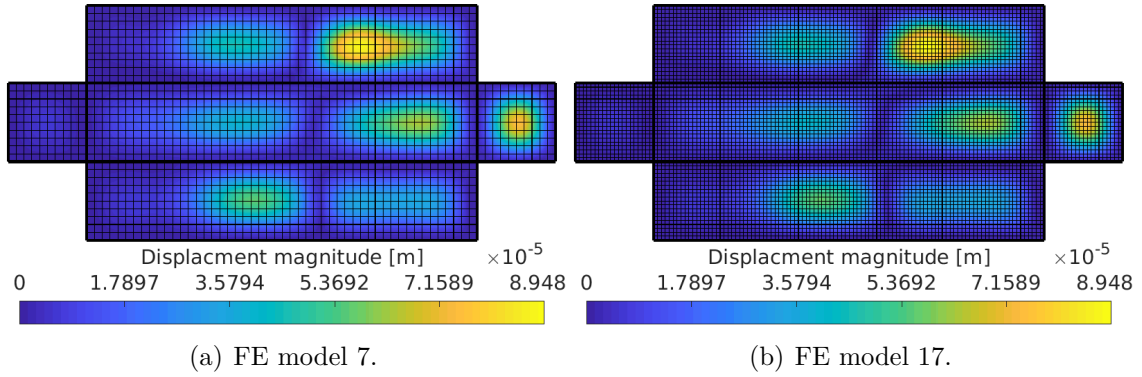

(a) FE model 7.

(b) FE model 17.

Figure 3.5: Static displacement magnitudes of the cavity with the CFD pressure distribution.

The relative errors of the displacement magnitudes were computed. The finest grid in each case was used for reference; thus, the error relative grid 21 was computed for the spatially uniform pressure distribution and grid 19 was used for reference for the CFD pressure distribution. The maximum displacements and the relative errors for the uniform distribution and the CFD distribution are shown in Figures 3.6 and 3.7, respectively.
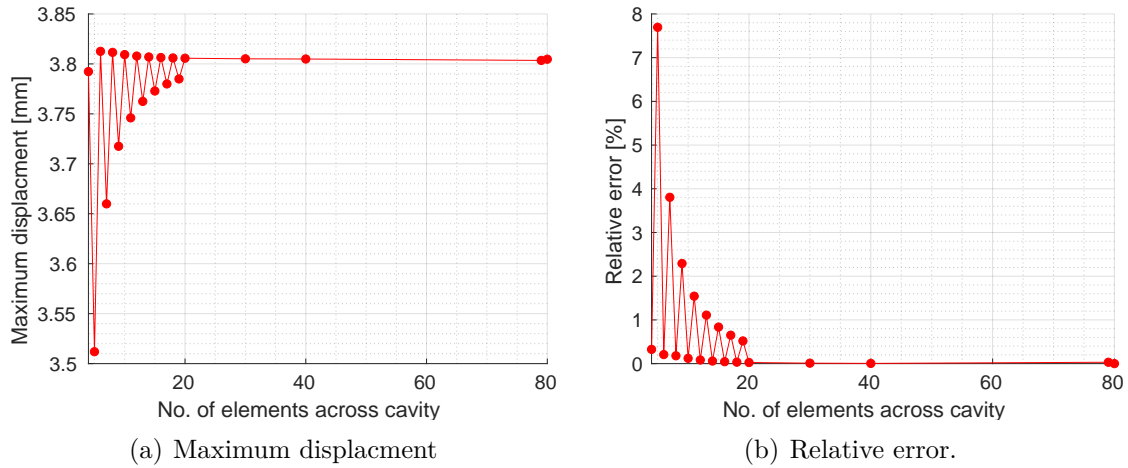

(a) Maximum displacment

(b) Relative error.

Figure 3.6: Maximum displacements and relative errors for the FE models with the spatially uniform pressure distribution.

The absolute magnitudes for the different distributions are large because of the large difference in pressure, however, the trends are similar. The maximum displacement and the relative error differ substantially depending on whether the number of elements across the width of the cavity is even or odd. If the number of elements are even, there are element nodes along the centrelines of the cavity walls, which is where the maximum displacement is expected. This trend would not be as apparent if second-order elements had been used, which allows for bending of the element

edges. The relative errors are generally smaller with the uniform pressure distribution. For all FE models with an even number and 8 or more elements across the cavity width, the relative error is less than a half percent for both pressure distributions.
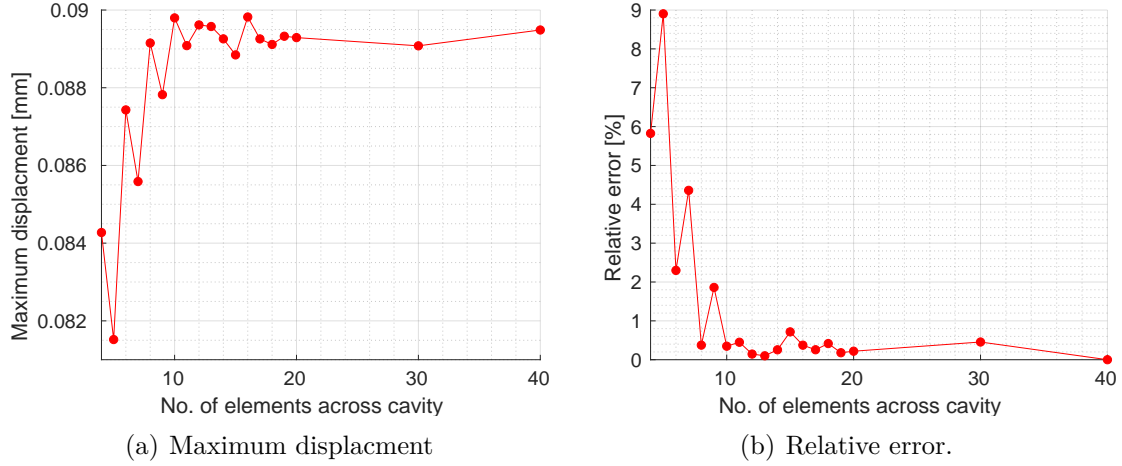

(a) Maximum displacment

(b) Relative error.

Figure 3.7: Maximum displacements and relative errors for the FE models with the CFD pressure distribution.

In addition to the aspects considered here, the eigenvectors and the associated eigenvalues may also change depending on the resolution of the FE model. This has not been investigated in detail for all the models presented here. However, it became relevant in Paper B where results using FE model 17 for the modal-based approach was compared with results using FE model 7 together with the non-modal approach. The normalised relative frequency difference (NRFD) and the modal assurance criterion (MAC) [38, 39] were computed for FE models 7 and 17 in Paper B, in order to compare the models.

3.2 Acoustic Analogy

Acoustic analogies are widely used to analyse far-field noise. The traditional aeroacoustic analogies are derived from the compressible Navier-Stokes equations, which are linearised to form an inhomogeneous wave equation. The first acoustical analogy was proposed by Lighthill [40, 41] in 1952–1954. Lighthill's analogy describes sound wave propagation in free space. Soon after, in 1955, Curle [42] incorporated the effect of solid walls into Lighthill's analogy. Come 1969, Ffowcs Williams and Hawkings (FW-H) [43] derived a generalised formulation of Lighthill's and Curle's theories and also expanded the theory to include moving solid walls. In the original formulation, a volume integration is required to include turbulent noise sources in the flow. The volume integration significantly increases the computational effort required. The volume integration can be replaced by a surface integration over permeable surfaces [44, 45], where the permeable surfaces should enclose all significant turbulent noise sources.

The foremost advantage of an acoustic analogy is the significantly reduced com-

putational effort required. Computational aeroacoustics (CAA) by means of conventional CFD is very challenging when it comes to far-field noise. A CFD grid is often highly stretched towards the far-field boundaries where the computational cells become large. This is not acceptable for far-field noise prediction; the whole distance between the noise sources and the far-field must be sufficiently resolved to avert non-physical dissipation of the acoustic waves. A much more efficient approach is to employ a hybrid CAA method involving CFD and an acoustic analogy. The near-field is computed with a suitable CFD technique. Afterwards, the far-field noise is computed with an acoustic analogy using source terms extracted from the CFD simulation.

3.2.1 Cavity Far-Field Noise

The hybrid CAA method is employed to predict the far-field noise resulting from the rigid and elastic cavity investigated in Paper A. The FW-H solver is an in-house code developed by Yao et al. [46] at Chalmers University of Technology. To isolate the effect of the elastic cavity, the source terms only encompass wall bounded quantities: pressure, grid velocity (zero for the rigid cavity), and coordinates (constant for the rigid cavity). Hence, the simulations are not intended to determine the total noise. The noise is computed at 146 observers, which are situated in three different planes according to Figure 3.8. It is worth noting that the distance from the origin to the xy-plane (red) observers are not the same as the observers in the other two planes. Contributions from the cavity walls and from the top surface are included in the simulation. For further details about the geometry, flow conditions, and CFD method the reader is referred to Paper A.
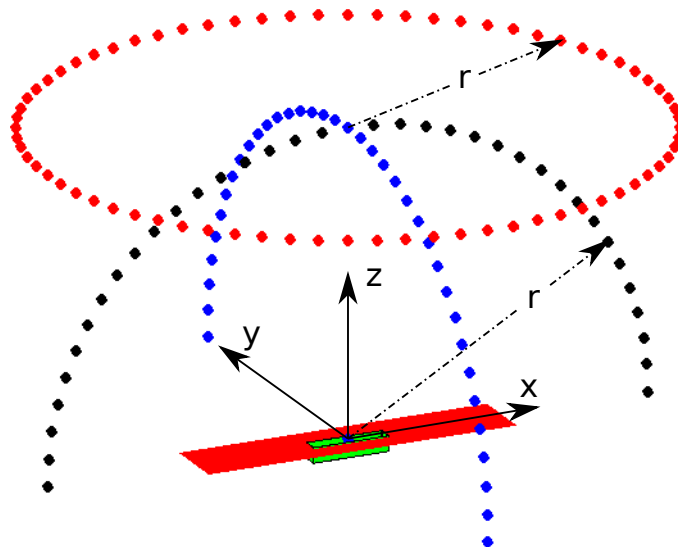

Figure 3.8: Black observers are in the xz-plane at $z = 0$, blue observers are in the yz-plane at $x = 0$, and red observers are in the xy-plane at $z = r = 40$ m. The cavity is coloured green and the top plate is red. The observers's location are not displayed in scale in relation to the cavity. The free-stream direction is in the $+x$-direction.

The time-averaged sound intensity I (energy flux) in the direction of propagation of an acoustic wave can be expressed as:

$$I = \frac{\overline{p'^2}}{\rho_0 c_0}. \tag{3.3}$$

Here, $\overline{p'^2}$ is the time-average of the pressure fluctuations squared. The characteristic impedance is $\rho_0 c_0$ [47], where ρ_0 and c_0 are the far-field fluid density and the speed of sound, respectively. The sound intensity at the observers for the rigid and elastic cavity are shown in Figure 3.9.
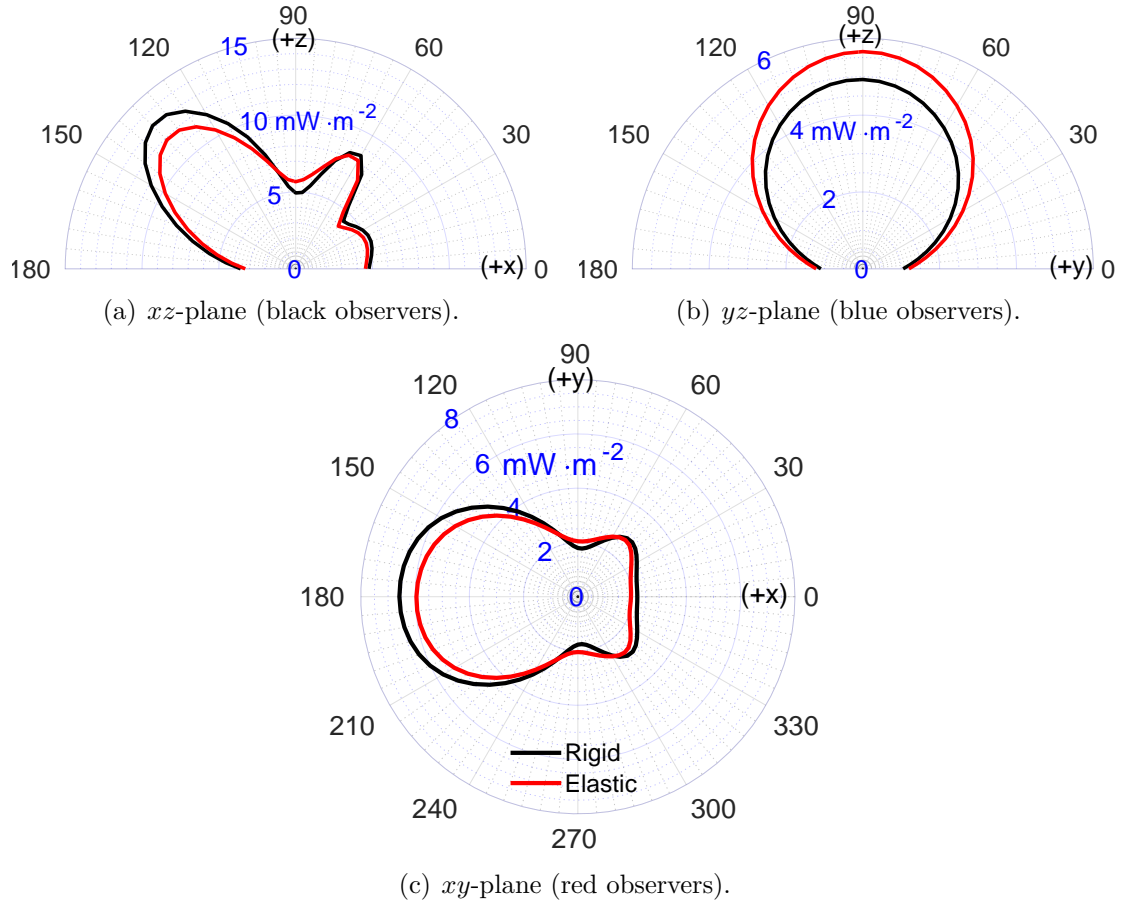

(a) xz-plane (black observers).

(b) yz-plane (blue observers).

(c) xy-plane (red observers).

Figure 3.9: Sound intensity I at the observers generated by the rigid and elastic cavity.

The rigid cavity generally results in a slightly higher sound intensity than the elastic cavity. The exception is in the yz-plane at $x = 0$, Figure 3.9 (b), where the intensity is higher for the elastic cavity; this can also be seen in Figure 3.9 (a) and (c). An intensity peak is obtained at about 60 degrees measured from the downstream direction as seen in Figure 3.9 (a). The highest intensity is obtained in the upstream direction at about 135 degrees (Figure 3.9 (a)).

The sound pressure level (SPL) for four of the observers in the xz-plane are shown in Figure 3.10. The Rossiter modes can clearly be identified in the spectra for the rigid cavity. In Paper A, it was reported that the 1st and 3rd Rossiter mode

energies were slightly lower for the elastic cavity, and that the 2nd Rositer mode was slightly higher. Furthermore, the energy of the 4th Rositer mode was depleted and a tone was induced at 816 Hz, also a tone at 900 Hz was intensified for the elastic cavity. These variations were obtained from the CFD simulation inside the cavity and also at microphones relatively close to the cavity. The variations are also obtained from the FW-H simulation shown in Figure 3.10. The induced tone in the elastic cavity at 816 Hz has the largest amplitude at 90 degrees in the xz-plane, shown in Figure 3.10 (b). This corresponds to the location where the sound intensity is larger for the elastic cavity than for the rigid cavity as shown in Figure 3.9.
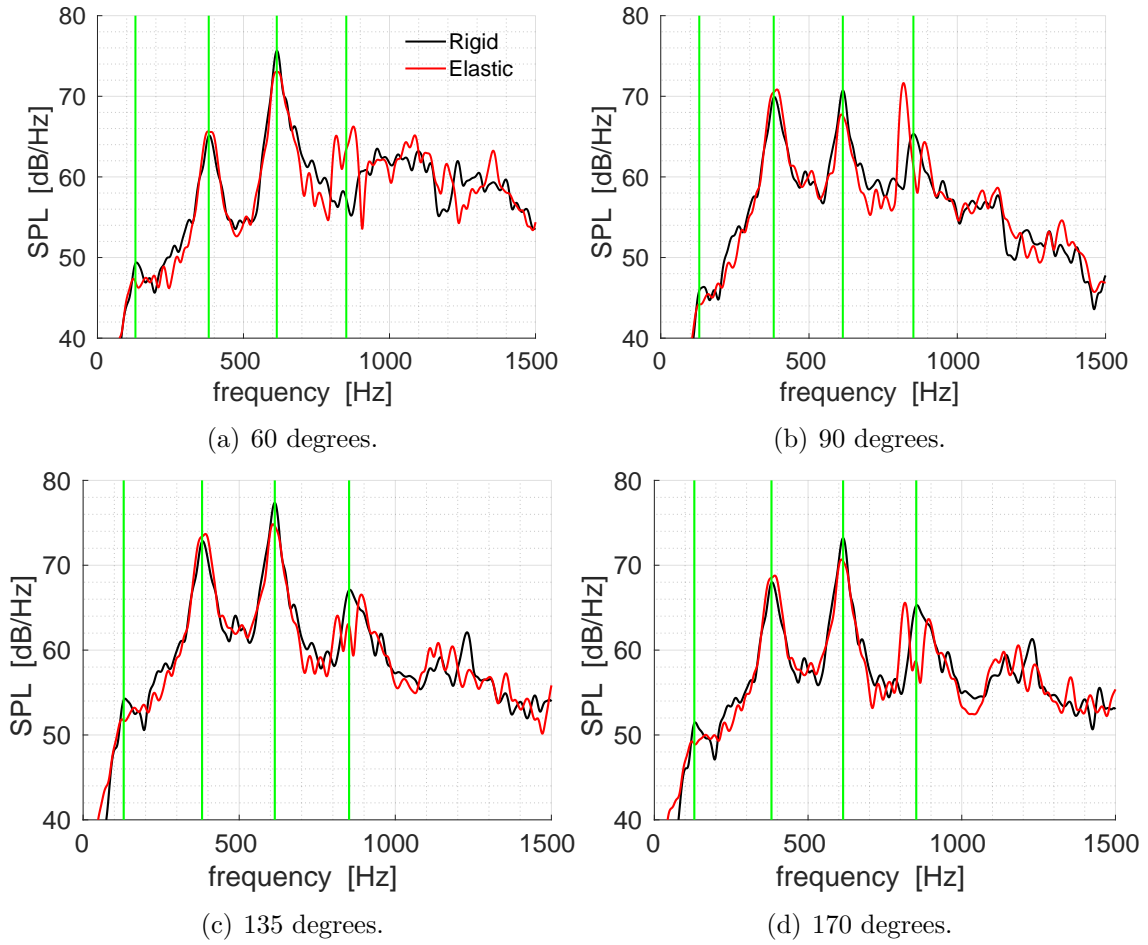

(a) 60 degrees.

(b) 90 degrees.

(c) 135 degrees.

(d) 170 degrees.

Figure 3.10: Sound pressure level in the xz-plane at $y = 0$, given angles are as according to Figure 3.9 (a). The green vertical lines mark the Rossiter frequencies.

Chapter 4

Aeroelastic Simulation of the ONERA M6 Wing

T his chapter presents a complementary study of the aeroelasticity of the ON-ERA M6 wing [48]. In Paper D, a difference in structural responses between URANS and DDES were obtained for cases where flow separation occurred, whereas the aeroelastic behaviour is near identical for attached flow. A difference in the aeroelastic behaviour is expected if the flow separates, research has shown that URANS does not suffice [15]. However, the hybrid RANS-LES simulations in Paper D suffered from deficiencies in the methodology that affected the results for the cases with detached flow. No experimental data of the aeroelasticity are available for the ONERA M6 wing and it is hence problematic to asses the validity of the aeroelastic behaviour. Nonetheless, the paucity of resolved turbulent structures evinces an inadequate methodology. This chapter presents a complementary study with an improved methodology for one of the cases where detached flow was obtained, namely case 18 in Table 3 in Paper D, that is, Mach 0.925 and a free-stream static pressure of 94 kPa. Results from simulations with hybrid RANS-LES and URANS on the rigid wing and the elastic wing are compared.

4.1   Methodology

If not stated otherwise, the same methodology is employed here as in Paper D. A finer computational grid is used, which is based on the previously used grid. The spatially grid resolution on the wing surface is increased as well as the wall-normal resolution. The maximum cell edge length at the wing-root is 3.6 mm and 2.0 mm at the wing tip. The total number of grid points is approximately 69 million. A cross-section of the grid at the wing-root is shown in Figure 4.1. Spalart-Allmaras improved delayed detached-eddy simulation (SA-IDDES) [23, 22] turbulence model together with a low-dissipation and low-dispersion second-order scheme [49] are employed. Spalart-Allmaras turbulence model [22] is also used for the URANS simulations. The time step is $1.0 \cdot 10^{-5}$ s. The rigid wing was first simulated with IDDES and URANS to examine the differences for the rigid wing. A total physical time of 0.3 s was simulated for the rigid wing, the latter 0.2 s is

presented here. As in Paper D, critical damping was first applied to the structure for the aeroelastic simulation. Subsequently, zero damping was used and an initial perturbation was applied to the second structural mode (1st pitch mode) to obtain the dynamic response.
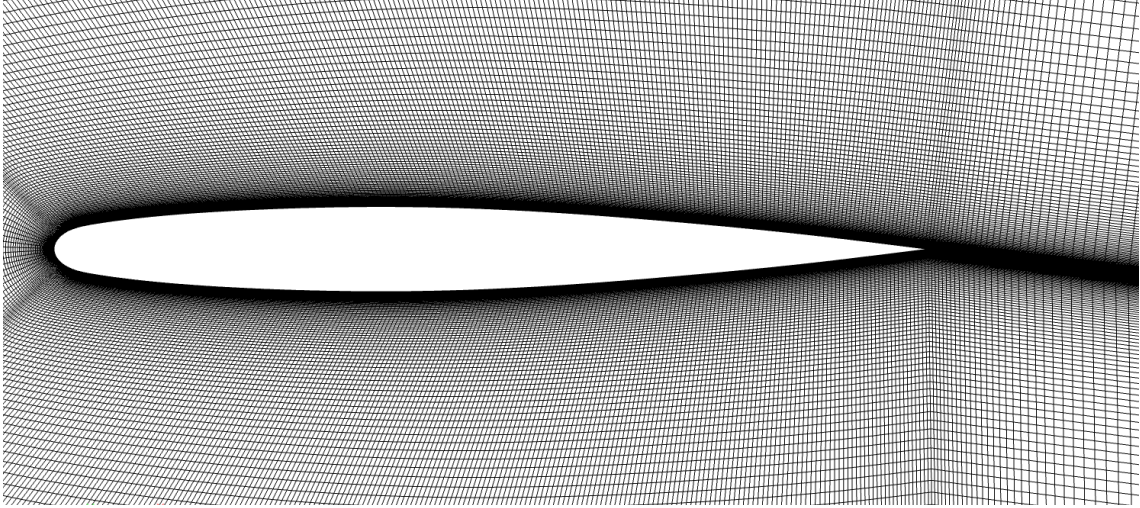

Figure 4.1: Cross-section of the computational grid at the wing-root.

4.2 Results

The ensuing sections present the results. First, results from the simulation with the rigid wing, followed by results from the aeroelastic simulation.

4.2.1 Rigid Wing

Figure 4.2 shows a visualisation of resolved turbulent structures using iso-surfaces of the Q-criterion [50]. Contrary to the results in Paper D, resolved turbulent structures are obtained. Figure 4.3 shows the time variation of the surface pressure coefficient for the rigid wing. The shock wave position using IDDES is throughout the wingspan upstream of the corresponding shock from the URANS simulation. Towards to the wing-root, Figure 4.3 (a)–(c), the shock wave is virtually stationary with URANS, whereas the movements of the shock are significant with IDDES. Towards the wing tip, the magnitudes of the movement of the shock wave are similar, but the shock is further upstream with the use of IDDES. Figure 4.4 shows the time-variation of the skin friction coefficient for the positions along the wingspan. The position of flow separation is generally further upstream for the IDDES simulation. The position of separation is indicated by the location where the skin friction coefficient first becomes negative. The shock wave position is close to the position of the flow separation. Solely based on these observations, it is to be expected that the static and dynamic responses of the elastic wing are different between IDDES and URANS.
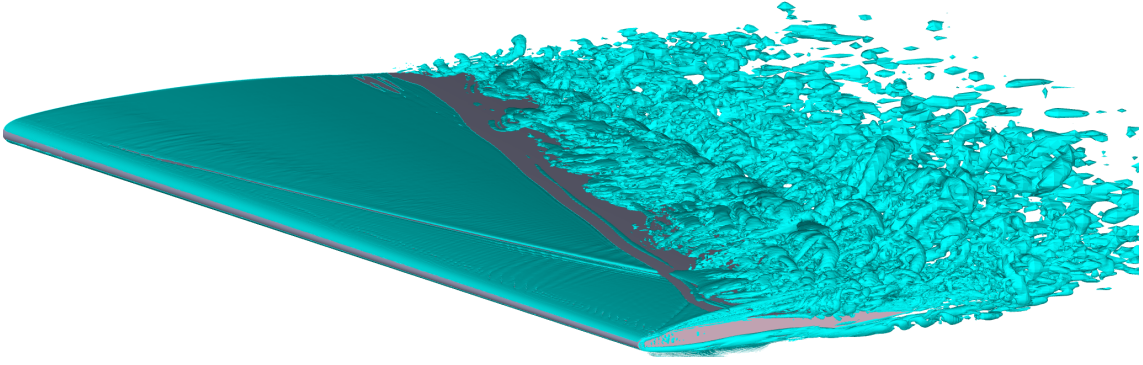
Figure 4.2: Visualisation of resolved turbulent structures using the Q-criterion.
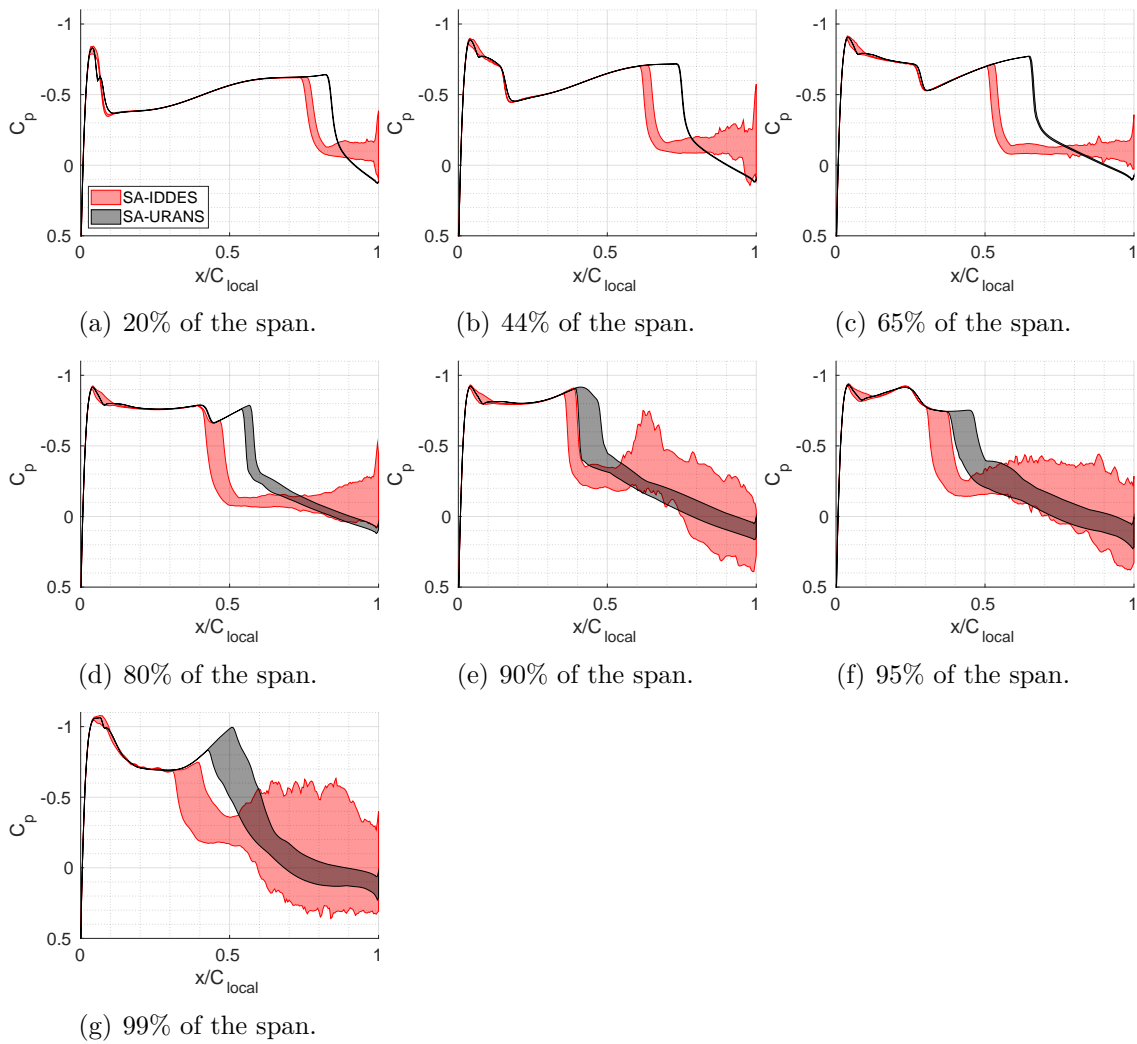

(a) 20% of the span.

(b) 44% of the span.

(c) 65% of the span.

(d) 80% of the span.

(e) 90% of the span.

(f) 95% of the span.

(g) 99% of the span.

Figure 4.3: Time variation ($t = 0.1$–0.3) of the surface pressure coefficient on the suction side of the rigid wing at 20–99 percent of the wingspan measured from the wing-root. The distance from the leading-edge is normalised by the local chord length.

(a) 20% of the span.

(b) 44% of the span.

(c) 65% of the span.

(d) 80% of the span.

(e) 90% of the span.

(f) 95% of the span.

(g) 99% of the span.

Figure 4.4: Time variation ($t = 0.1$–0.3) of the x-directional skin friction coefficient on the suction side of the rigid wing at 20–99 percent of the wingspan measured from the wing-root. The distance from the leading-edge is normalised by the local chord length.
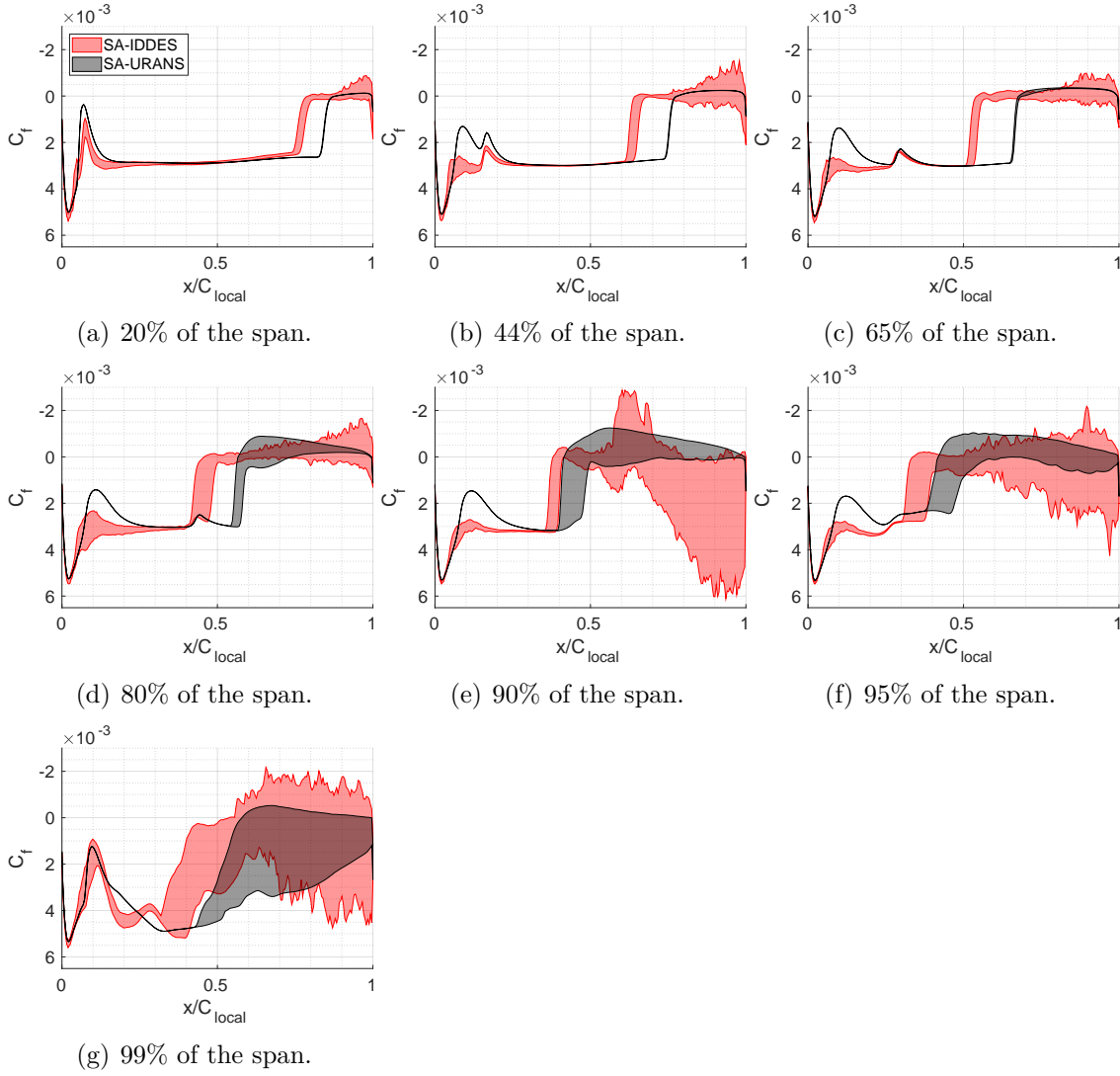
4.2.2 Aeroelastic Wing

The static and dynamic aeroelastic responses are shown in Figure 4.5. The first 0.25 s of the signals show the static response of the plunge and pitch (defined in Paper D) at the wing tip. The difference between IDDES and URANS is significant. Since the shock wave is further upstream for IDDES, there is a larger area with high pressure acting on the suction side of the wing. This causes the pitch to be greater (higher angle-of-attack) for IDDES. The higher pressure also causes the the plunge (bending) of the wing to be smaller for IDDES compared with URANS. The dynamic responses ($0.25 < t < 1.25$ s) are dissimilar. The amplitude of the oscillations is much greater for IDDES than for URANS. The plunge oscillations constitutes more high frequency content, which is an indication of that the IDDES prediction is closer

to the flutter boundary than the URANS prediction. It can an also be inferred from the oscillations that the damping is lower for IDDES than for URANS, which implies that the IDDES simulation is closer to the flutter boundary.
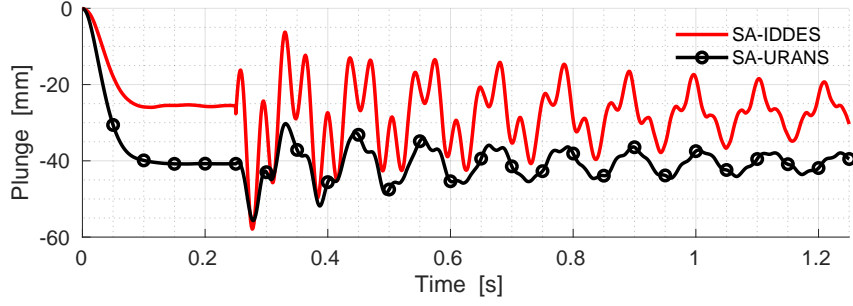
(a)
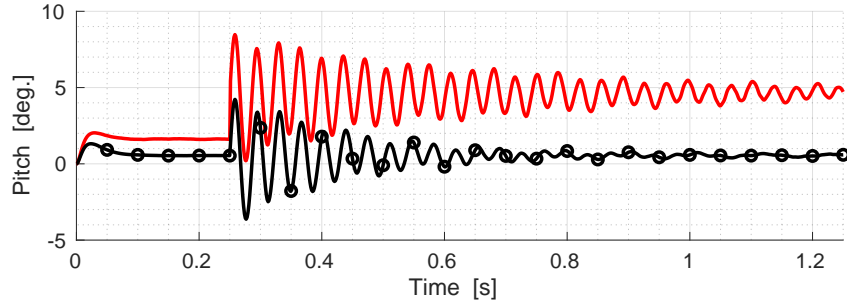
(b)

Figure 4.5: Static ($0 < t < 0.25$ s) and dynamic ($0.25 < t < 1.25$ s) plunge and pitch responses.
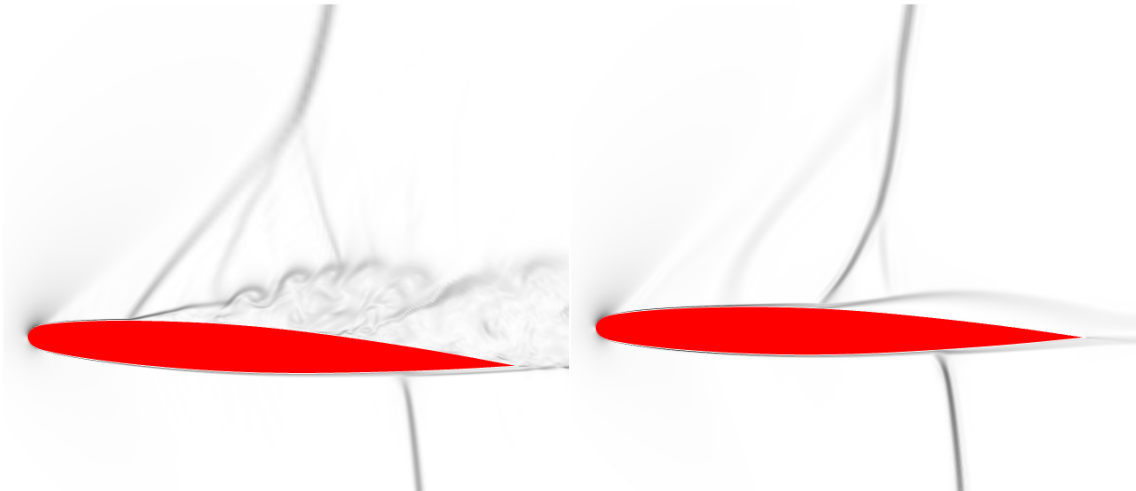

Figure 4.6: Instantaneous density gradient at time $t = 0.5415$ s at 95 percent of the wingspan. **Left:** IDDES. **Right:** URANS.

Figure 4.6 shows the instantaneous density gradient at time $t = 0.5415$ s. For IDDES, resolved turbulence is clearly seen downstream of the shock where the flow separates. A separation downstream of the shock is also obtained with URANS.

Chapter 5

Summary

T his chapter summarises the appended papers and the work undertaken in this project. The first section summarises the papers on cavity flow and the following summarises the paper and complimentary study on the aeroelastic wing. Each section ends with some concluding remarks and future work is briefly discussed.

5.1 Cavity Flow

5.1.1 Paper A

Effects of Aeroelastic Walls on the Aeroacoustics in Transonic Cavity Flow

The paper presents a novel study on the effects of elastic cavity walls on the aeroacoustics at a transonic Mach number of 0.85. The M219 cavity geometry is used, for which experimental data are available for the rigid cavity. A flow solver validation is undertaken for the rigid cavity, where SA-DDES and SA-IDDES are assessed. Overall, the SA-IDDES is deemed to better predict the Rossiter modes and is used for the FSI simulation. The grey area effect is less apparent with SA-IDDES as compared to SA-DDES, because of the faster transition from modelled stresses in RANS mode to resolved stresses in LES mode.

Only the aerodynamics of the M219 cavity has been measured in a wind tunnel and no aeroelastic data are available. Instead, the effects of the elastic cavity walls are investigated by comparing the results with corresponding quantities from a rigid cavity simulation. The modal-based approach is employed. The modal basis was truncated after the 50th normal mode shape, including eigenfrequencies up to approximately 2300 Hz. A spectral analysis is performed for the pressure fluctuations in a microphone array that is situated in the flow above the cavity. Spectral proper orthogonal decomposition (SPOD) [51, 52] is employed to analyse cavity wall pressure fluctuations and wall displacements. The spectra of both analyses show a depletion of the energy at the 4th Rossiter mode frequency in the elastic cavity. A strong tone is concurrently induced at a frequency slightly below the 4th Rossiter mode frequency, which is not present in the rigid cavity.

5.1.2 Paper B

Effects of Aeroelastic Walls on the Aeroacoustics in Transonic Cavity Flow, Utilising a non-Modal Approach

The same elastic cavity problem as in Paper A is investigated. The methodology employed is similar to the one used in Paper A, with the exception that a non-modal approach is employed for structural simulation. A reduced order finite element model is used. An analytical selection scheme is used for the selection of master degrees-of-freedom. The scheme ensures that all significant eigenmodes are retained in the reduced order model. As in Paper A, the signals from a microphone array are analysed, and a SPOD analysis is performed for wall pressures and wall displacements. In addition to the depletion of energy at the 4th Rossiter mode and the induced tone below the 4th Rossiter mode, another strong tone above the 4th Rossiter mode frequency is obtained. The absence of the tone in the modal-based simulation is due to the method, or the truncation error of the method.

5.1.3 Paper C

Conjunction of Aeroelasticity and Aeroacoustics in Transonic Cavity Flow

Paper A is an extended version of this conference paper.

5.1.4 Concluding Remarks

The investigation of the elastic cavity shows the potential importance of considering the aeroelasticity in cavity flow. The studies show that the acoustic field is altered by means of aeroelasticity. Whether the aeroelasticity is important or not also depends on which questions should be answered, and on the cavity design. It should be stressed that it is a single case of an ideal cavity that has been investigated; it is hence not possible to draw a general conclusion that is valid for all cavities. The fluid-structure interaction is bidirectional and it has been shown that the spectral pressure distribution on the cavity walls are different in the elastic cavity. Hence, it may be of importance to consider the aeroelasticity for the prediction of structural stability and fatigue.

The flow solver validation evinced that improvements of the hybrid RANS-LES methods are desired. The accurate prediction of the Rossiter modes becomes especially important as they interact with the structural modes. Therefore, for future work, it would be important with further methodology studies on flow simulation of the flow in the rigid cavity, for which experimental data are available. It would also be highly desirable to have validation data from a wind tunnel test, for which aeroelastic walls are considered. Further studies of the structural methods and the coupling between the flow solver and the structural solver are also needed, to gain insights to the potential effects and level of accuracy.

Further investigation into the results of the already performed simulations can also be made to comprehend and explain the interaction.

5.2   Aeroelastic Wing

5.2.1   Paper D

Effects of Viscosity and Density on the Aeroelasticity of the ONERA M6 Wing from Subsonic to Supersonic speeds

This paper presents a study of the viscous effects on the aeroelastic prediction of a wing. The ONERA M6 wing geometry is used. Mach numbers from 0.6 to 1.1 are simulated. Simulations with the SA-DDES turbulence model and simulations with the inviscid Euler equations (IEE) are performed. The static and dynamic structural responses from the viscous and inviscid flow simulations are examined and compared. A few of the cases are also simulated with URANS. The modal-based approach is employed for the structural simulation. All Mach numbers are simulated with a constant free-stream density and, additionally, higher free-stream densities in order to find the critical dynamic pressure where aerodynamic flutter is obtained. A significant difference in the aeroelastic responses is found for Mach numbers between 0.875 and 0.950 for the SA-DDES and the IEE simulations. For attached flow, SA-DDES provides a response near identical to that of URANS, as expected. The cases with detached flow, caused by a shock induced separation, a substantial difference in the responses is obtained. However, the methodology employed suffered from a few weaknesses, which resulted in a lack of resolved turbulence in the SA-DDES simulations.

5.2.2   Concluding Remarks

The methodology was improved in Chapter 4 where the wing was simulated with SA-IDDES and unsteady RANS for a case with detached flow. The simulations of the rigid wing showed a significant difference in the surface pressure distribution between the flow simulation methods. The static and dynamic aerodynamic responses were substantially dissimilar. Unfortunately, there are no aeroelastic data for the simulated case. Hence, it is not possible to conclude that the predictions made in Chapter 4 are accurate. A grid convergence study could be performed to, to some extent, validate the method.

Hybrid RANS-LES simulations of separated wall-bounded flows are generally very challenging. Moreover, the accuracy of the flow simulation is a prerequisite for accurate prediction of the structural response. Even though the greatest challenge comes from the flow simulation there are other potential sources of error, which have not been investigated here. For instance, the method for structural simulation and the coupling between the solvers. Furthermore, for real-world problems the accuracy of the structural model is essential. Even though a structure has isotropic material properties, an assembled real-world structure may be non-linear, which understandably pose a problem for linear structural solvers.

Bibliography

[1] E. B. Plentovich, R. L. Stallings Jr., and M. B Tracy. Experimental Cavity Pressure Measurements at Subsonic and Transonic Speeds. *NASA, Technical Paper 3358*, 1993.

[2] A. Roshko. Some measurements of flow in a rectangular cutout. *N.A.C.A. Technical Note no. 3488*, 1955.

[3] K. Krishnamurty. Acoustic radiation from two-dimentional rectangular cutouts in aerodynamic surfaces. *N.A.C.A. Technical Note no. 3487*, 1955.

[4] W. H. Dunham. Flow induced cavity resonance in viscous compressible and incompressible fluids. *4th Symp. Naval Hydrody. Propulsion Hydroelasticity, paper ACR-92*, pages 1057–1081, 1962.

[5] H. E. Plumblee, J. S. Gibson, and L. W. Lassiter. A Theoretical and Experimental Investigation of the Acoustic Response of Cavities in an Aerodynamic Flow. *Technical report no. WADD-61-75, USAF*, 1962.

[6] J. E. Rossiter. Wind tunnel experiments of the flow over rectangular cavities at subsonic and transonic speeds. *Reports and Memoranda No. 3438, Ministry of Aviation; Her Majesty's Stationery Office: London, UK*, 1966.

[7] L. F. East. Aerodynamically induced resonance in rectangular cavities. *Journal of Sound and Vibration*, 3:277–287, 1966.

[8] C. K. W. Tam and P. J. W Block. On the tones and pressure oscillations induced by flow over rectangular cavities. *Journal of Fluid Mechanics*, 89(2):373–399, 1978.

[9] M. A. Kegerise, E. F. Spina, S. Garg, and L. Cattafesta. Mode-switching and Nonlinear Effects in Compressible Flow Over a Cavity. *Physics of Fluids*, 16(3):678–687, 2004.

[10] G. J. M. Loupy and G. N. Barakos. Understanding Transonic Weapon Bay Flows. *In: 6th European Conference on Computational Mechanics (ECCM 6) 7th European Conference on Computational Fluid Dynamics (ECFD 7), Glasgow, UK, 11–15 June 2018*, 2018.

[11] S. Nilsson, H. D. Yao, A. Karlsson, and S. Arvidson. Effects of Aeroelastic Walls on the Aeroacoustics in Transonic Cavity Flow. *Aerospace*, 9(716), 2022.

[12] S. Nilsson, H. D. Yao, A. Karlsson, and S. Arvidson. Effects of Aeroelastic Walls on the Aeroacoustics in Transonic Cavity Flow, Utilising a non-Modal Approach. *Technical report*, 2022.

[13] S. Nilsson, H. D. Yao, A. Karlsson, and S. Arvidson. Conjunction of Aeroelasticity and Aeroacoustics in Transonic Cavity Flow. *In Proceedings of the International Forum on Aeroelasticity and Structural Dynamics (IFASD), Madrid, Spain, 13–17 June 2022, Paper No. IFASD-2022-020*, 2022.

[14] H. Babinsky and J. K. Harvey. Shock Wave-Boundary-Layer Interactions. *Cambridge University Press, 32 Avenue of the Americas, New York, NY 10013-2473, USA*, 2011.

[15] J. Heeg, P. Chwalowski, D. Schuster, and M. Dalenbring. Overview and lessons learned from the Aeroelastic Prediction Workshop. *54th AIAA/ASME/ASCE/AHS/ASC Structures, Structural Dynamics, and Materials Conference*, 2013.

[16] E. H. Dowell. A Modern Course in Aeroelasticity. *Springer, Gewerbestrasse 11, 63 30 Chamm Switzerland*, 2015.

[17] S. Nilsson, H. D. Yao, A. Karlsson, and S. Arvidson. Effects of Viscosity and Density on the Aeroelasticity of the ONERA M6 Wing from Subsonic to Supersonic Speeds. *In Proceedings of the AIAA Aviation forum, Chicago, IL, USA, 27 June–1 July 2022, paper no. AIAA 2022-3670*, 2022.

[18] M. Carlsson. Towards Improved Scale-Resolving Modeling and Simulations of Turbulent Flows. *PhD thesis 2022, Chalmers University of Technology, ISBN 978-91-7905-740-4*, 2022.

[19] S Arvidson. Methodologies for RANS-LES interfaces in turbulence-resolving simulations. *PhD thesis 2017, Chalmers University of Technology, ISBN 978-91-77597583-2*, 2017.

[20] C Mockett, W. Haase, and F. Thiele. Go4hybrid: A European Initiative for Improved Hybrid RANS-LES Modelling. *In S. Girimaji, W. Haase, S-H. Peng, and D. Schwamborn, editors, Progress in Hybrid RANS-LES Modelling, Springer International Publishing*, 130:299–303, 2015.

[21] P. Spalart, S. Deck, M. Shur, K. Squires, M. K. Strelets, and A. Travin. A new version of detached-eddy simulation, resistant to ambiguous grid densities. *Theory of Computational Fluid Dynamics*, 20:181–195, 2006.

[22] P. Spalart and S. Allmaras. A One-Equation Turbulence Model for Aerodynamic Flows. *La Recherche Aérospatiale*, 1:5–21, 1994.

[23] M. L. Shur, P. R. Spalart, M. K. Strelets, and A. K. Travin. A hybrid RANS-LES approach with delayed-DES and wall-modelled LES capabilities. *International Journal of Heat and Fluid Flow*, 29:1638–1649, 2008.

[24] R. R. Jr Craig and M. C. C. Bampton. Coupling of substructures for dynamic analyses. *AIAA Journal*, 6(7):1313–1319, 1968.

[25] R. Guyan. Reduction of stiffness and mass matrices. *AIAA Journal*, 3(2):380, 1965.

[26] Z.-Q. Qu. *Model Order Reduction Techniques : with Applications in Finite Element Analysis*. Springer-Verlag London, 2004.

[27] O. Flodén, K. Persson, and G. Sandberg. Reduction methods for the dynamic analysis of substructure models of lighweight building structures. *Computers and Structures*, 138:49–61, 2014.

[28] R. Levy. Guyan reduction solutions recycled for improved accuracy. *NASTRAN Users Experiences*, pages 201–220, 1971.

[29] J.N Ramsden and J.R. Stoker. Mass condensation - a semi-automatic method for reducing the size of vibration problems. *International Journal for Numerical Methods in Engineering*, 1(4):333–349, 1969.

[30] N. Popplewell, A.W.M Bertels, and B Arya. A critical appraisal of the eliminating technique. *Journal of Sound and Vibration*, 31(2):213–233, 1973.

[31] V.N Shah and M. Raymund. Analytical selection of masters for the reduced eigenvalue problem. *International Journal for Numerical Methods in Engineering*, 18(1):89–98, 1982.

[32] K.W Matta. Selection of degrees of freedom for dynamic analysis. *Journal of Pressure Vessel Technology*, 109(1):65–69, 1987.

[33] L.E. Suarez and M.P. Singh. Dynamic condensation method for structural eigenvalue analysis. *AIAA Journal*, 30(4):1046–1054, 1992.

[34] N. Bouhaddi, S. Cogan, and R. Fillod. Dynamic substructuring by Guyan condensation selection of the master DOF. *Proceedings of the 10th International Modal Analysis Conference (San Diego, CA), Society for Experimental Mechanics*, pages 328–333, 1992.

[35] N. Bouhaddi and R. Fillod. A method for selecting master DOF in dynamic substructuring using the Guyan condensation method. *Computers and Structures*, 45(5/6):941–946, 1992.

[36] M. J. de Henshaw. M219 Cavity Case, Verification and Validation Data for Computational Unsteady Aerodynamics. *British Aerospace (Operations) Ltd, Military Aircraft and Aerostructures*, 1991.

[37] MSC Software Corporation. MSC Nastran 2012.2, Quick Reference Guide. *2 MacArthur Place Santa Ana, USA*, 2012.

[38] R. J. Allemang and D. L. Brown. Correlation coefficient for modal vector analysis. *In Proceedings of the International Modal Analysis Conference and exhibit, Orlando, Florida, USA, 8–10 November 1982*, 1982.

[39] R. J. Allemang. The modal assurance criterion—twenty years of use and abuse. *Sound and Vibration*, 37:14–23, 2003.

[40] M. J. Lighthill. On sound generated aerodynamically. I. General theory. *Proc. of the Royal Society of London, Series A, Mathematical and Physical Sciences*, 211(1107):564–587, 1952.

[41] M. J. Lighthill. On sound generated aerodynamically. II. Turbulence as a source of sound. *Proc. of the Royal Society of London, Series A, Mathematical and Physical Sciences*, 222(1148), 1954.

[42] N. Curle. The influence of solid boundaries upon aerodynamic sound. *Proc. of the Royal Society of London, Series A*, 231(1187):505–514, 1955.

[43] J.E. Ffowcs Williams and D. L. Hawkings. Sound generation by turbulence and surfaces in arbitrary motion. *Philosophical Transactions of the Royal Society of London, Series A, Mathematical and Physical Sciences*, 264(1151):321–342, 1969.

[44] P. D. Francescantonio. A new Kirchhoff formulation for transonic rotor noise. *Journal of Sound and Vibration*, 202:491–509, 1997.

[45] K. S. Brentner and F Farassat. An analytical comparison of the acoustic analogy and Kirchhoff formulation for moving surfaces. *AIAA Journal*, 36:1379–1386, 1998.

[46] H. D. Yao, L. Davidson, L. E. Eriksson, S. H. Peng, O. Grundestam, and P. E. Eliasson. Surface integral analogy approaches for predicting noise from 3D high-lift low-noise wings. *50th AIAA Aerospace Sciences Meeting*, (2012-0386), 2012.

[47] S. W. Rienstra and A. Hirschberg. An introduction to Acoustics. *Eindhoven University of Technology*, 2020.

[48] V. Schmitt and F. Charpin. Pressure distributions on the ONERA-M6-Wing at transonic Mach numbers, Experimental Data Base for Computer Program Assessment. *Report of the Fluid Dynamics Panel Working Group 04, AGARD AR 138*, 1979.

[49] J. Löwe, A. Probst, T. Knopp, and R. Kessler. Low-dissipation low-dispersion second-order scheme for unstructured finite-volume flow solvers. *AIAA Journal*, 54, 2016.

[50] J. C. R. Hunt, A. Wray, and P. Moin. Eddies, streams, and convergence zones in turbulent flows. *In Proceedings of the Summer Program, Center for Turbulence Research, Stanford University*, pages 193–208, 1988.

[51] A. Towne, O. T. Schmidt, and T. Colonius. Spectral proper orthogonal decomposition and its relationship to dynamic mode decomposition and resolvent analysis. *Journal of Fluid Mechanics*, 847:821–867, 2018.

[52] A. Nekkanti and O. T. Schmidt. Frequency-time analysis, low-rank reconstruction and denoising of turbulent flows using SPOD. *Journal of Fluid Mechanics*, A26 DOI 10.1017/jfm.2021.681(926), 2021.

Bibliography